ACCSCIENCE PUBLISHING

International Journal of Bioprinting

RESEARCH ARTICLE

Three-dimensional-printed hydrogel scaffolds with neuregulin-1 sustained-release microspheres for enhanced dedifferentiation and myelin regeneration in peripheral nerve injury

Guanhua Zhang[1†], Enpeng Song[2†], Peng Yu[1†], Jie Wei[3], Yaqiong Wang[4*], Jie Liu[5*], and Hou Bo[2*]

[1]Department of Cerebrovascular Surgery, The Third Affiliated Hospital of Sun Yat-sen University, Guangzhou, Guangdong, China

[2]Department of Neurosurgery, Lingnan Hospital, The Third Affiliated Hospital of Sun Yat-sen University, Guangzhou, Guangdong, China

[3]Department of Pediatrics, School of Pediatrics, Guangzhou Medical University, Guangzhou, Guangdong, China

[4]Department of Electron Microscopy, Zhongshan School of Medicine, Sun Yat-sen University, Guangzhou, Guangdong, China

[5]Department of Neurosurgery, Hezhou People's Hospital, Guangxi, China

[†]These authors contributed equally to this work.

***Corresponding authors:**
Yaqiong Wang
(wangyaq2@mail.sysu.edu.cn)

Jie Liu
(liuj616@163.com)

Hou Bo
(houb@mail.sysu.edu.cn)

Citation: Zhang G, Song E, Yu P, *et al.* Three-dimensional-printed hydrogel scaffolds with neuregulin-1 sustained-release microspheres for enhanced dedifferentiation and myelin regeneration in peripheral nerve injury. *Int J Bioprint.* 2025;11(5):154-177. doi: 10.36922/IJB025170168

Received: April 26, 2025
1st revised: May 31, 2025
2nd revised: June 11, 2025
Accepted: June 16, 2025
Published Online: June 16, 2025

Abstract

Remyelination is critical for functional recovery following peripheral nerve injury. Although autologous Schwann cell transplantation promotes effective myelin repair, its clinical translation remains limited due to donor scarcity and associated morbidity. Bone marrow-derived Schwann-like cells (B-dSCs) offer a promising alternative; however, their limited dedifferentiation capacity significantly constrains therapeutic outcomes. Neuregulin-1 (NRG1), a key axonal signal, effectively induces Schwann cell dedifferentiation but requires precise, sustained delivery to exert optimal effects. Here, we developed a three-dimensional (3D)-printed hydrogel scaffold incorporating NRG1-loaded sustained-release microspheres to achieve localized, prolonged NRG1 delivery. *In vitro* studies demonstrated that NRG1 significantly enhanced the dedifferentiation and remyelination capacity of B-dSCs in a dorsal root ganglion co-culture system. Mechanistically, NRG1 promoted dedifferentiation by activating the c-Jun N-terminal kinase (JNK) signaling pathway—a pivotal regulator of Schwann cell plasticity. Pharmacological inhibition of JNK markedly suppressed NRG1-induced dedifferentiation and downregulated myelin-associated gene expression, confirming pathway specificity. Furthermore, the 3D-printed scaffold effectively maintained uniform NRG1 distribution, facilitating enhanced axonal regeneration and improved myelin integrity. Collectively, these findings highlight the essential role of JNK signaling in NRG1-driven Schwann cell dedifferentiation and underscore the therapeutic promise of combining sustained-release systems with engineered cell therapies to advance peripheral nerve repair.

Keywords: C-Jun N-terminal kinase pathway; Dedifferentiation; Neuregulin-1; Peripheral nerve injury; Schwann cells; Sustained-release microspheres

1. Introduction

Peripheral nerve injury (PNI) is a major global health issue, and successful remyelination is critical for functional nerve repair.[1,2] Autologous Schwann cell (ASC) transplantation has shown considerable promise in enhancing myelin regeneration[3,4]; however, harvesting ASCs from functional nerves often leads to significant donor-site morbidity.[5] To address this challenge, Schwann-like cells derived from bone marrow mesenchymal stem cells (BMSCs), termed bone marrow-derived Schwann-like cells (B-dSCs), have emerged as a promising alternative.[6] Although these cells share key functional properties with ASCs and are more accessible, our previous studies identified a critical limitation: B-dSCs exhibit insufficient dedifferentiation capacity, leading to suboptimal *in vivo* myelination compared to ASCs.[7] Therefore, strategies to enhance B-dSC dedifferentiation are urgently needed to fully harness their therapeutic potential.

Dedifferentiation refers to the phenotypic reversion of Schwann cells to a "repair" state in response to injury-induced signals following PNI.[8,9] This transition is characterized by cytoskeletal remodeling, the adoption of bipolar or multipolar morphologies, and the reacquisition of high motility and neurotrophic factor secretion.[10] Given that dedifferentiation is essential for initiating remyelination, impaired dedifferentiation significantly hampers nerve regeneration.[11,12] Current strategies aimed at promoting Schwann cell dedifferentiation include chemical stimulation, gene editing, and the use of bioactive molecules such as tumor necrosis factor (TNF), interleukins (ILs), and neuregulin-1 (NRG1).[13–15] However, chemical and genetic approaches often lack specificity or raise safety concerns, while TNF and ILs primarily activate inflammatory or apoptotic pathways, potentially causing adverse effects.[16–21]

In contrast, NRG1, an endogenous nervous system protein, offers excellent biocompatibility and a strong affinity for Schwann cells.[22,23] After nerve injury, NRG1 critically orchestrates Schwann cell dedifferentiation via activation of the mitogen-activated protein kinase signaling pathways, notably through the v-erb-b2 avian erythroblastic leukemia viral oncogene homolog 2/3 receptors, leading to downstream activation of c-Jun N-terminal kinase (JNK), a central regulator of Schwann cell plasticity.[24–26] Activation of JNK promotes Schwann cell transition into the repair phenotype by inhibiting myelin-related gene expression and upregulating dedifferentiation markers such as c-Jun.[27] *In vivo*, inhibition of the JNK pathway impairs the formation of repair Schwann cells, emphasizing the indispensable role of JNK signaling in demyelination-regeneration cycles.[28] Thus, sustained NRG1 delivery presents a promising mechanism to overcome intrinsic dedifferentiation limitations of B-dSCs through persistent JNK pathway activation.

Nevertheless, the protracted nature of nerve regeneration and the anatomical complexity necessitate sustained and localized delivery of NRG1 at the injury site. Current delivery strategies—including subcutaneous injections, engineered cell therapies, and biomaterial-based protein release—often fail to maintain optimal NRG1 concentrations over extended periods.[29–31] Although hydrogels and other biomaterials are widely used, they generally provide limited sustained-release capabilities.[32–35] Additionally, due to its inherent water solubility, NRG1 is prone to diffusion, enzymatic degradation, and rapid clearance.[36,37] In previous work, we encapsulated NRG1 within sustained-release microspheres (NRG1-SRMs) to prolong its release and improve stability.[38] However, traditional hydrogel matrices lack sufficient structural constraints, resulting in microsphere sedimentation and uneven NRG1 distribution.[39]

To address this limitation, we developed a composite gelatin/sodium alginate hydrogel system. Gelatin provides favorable biocompatibility and cell adhesion properties, while sodium alginate contributes mechanical stability and mild gelation capability. This material combination is ideally suited for precise three-dimensional (3D) printing, allowing for controlled scaffold architecture and uniform microsphere integration. Our previous work confirmed this hydrogel's capability for sustained bioactive factor release and tissue regeneration.[7]

Building upon this composite system, we utilized advanced 3D printing technology to fabricate highly organized, grid-like scaffolds composed of interconnected hydrogel fibers. This structural design allows for the physical entrapment of NRG1-SRMs within individual hydrogel fibers, effectively preventing microsphere aggregation and ensuring homogeneous NRG1 distribution throughout the scaffold.

In summary, this study investigates the hypothesis that embedding NRG1-SRMs within 3D-printed composite hydrogel scaffolds enhances B-dSC dedifferentiation and improves their *in vivo* myelination efficacy. Our findings offer novel mechanistic insights and propose advanced biomaterial strategies for improving therapeutic outcomes in peripheral nerve repair.

2. Materials and methods

2.1. Animals

Newborn Sprague–Dawley rats (3–5 days old; n=21) were used for the isolation of BMSCs, while adult female

Sprague–Dawley rats (weighing 180–200 g; *n*=90) were used to establish the PNI model and to isolate ASCs. All animals were housed under a 12-h light/dark cycle with *ad libitum* access to food and water and were acclimatized for at least 7 days prior to experimentation. The animals were obtained from the Laboratory Animal Center of the Sun Yat-sen University School of Medicine. All experimental procedures were approved by the Institutional Animal Care and Use Committee (IACUC) of Sun Yat-sen University and conducted in accordance with the Guide for the Care and Use of Laboratory Animals issued by the Chinese Institute of Health.

2.2. Preparation of neuregulin-1-loaded sustained-release microspheres

To prepare NRG1-SRMs, NRG1 (R1866r, EIAab Science, China), dextran (molecular weight 67 kDa; Sigma-Aldrich, USA), and polyethylene glycol (PEG; molecular weight 8000; Sigma-Aldrich, USA) were mixed at a mass ratio of 1:5:50. The mixture was stirred for 1 min and subsequently stored at −80°C for 12 h. It was then subjected to vacuum freeze-drying. The resulting lyophilized powder was washed with dichloromethane (Sigma-Aldrich, USA) and centrifuged. The supernatant, containing PEG, was collected, and the solvent was evaporated to obtain NRG1-loaded dextran microspheres.

These microspheres were suspended in 15% polylactic-co-glycolic acid (PLGA) dissolved in dichloromethane and subsequently emulsified in an aqueous solution containing 1% polyvinyl alcohol and 5% sodium chloride. The protein–dextran–PLGA emulsion was then solidified, hardened, freeze-dried, and stored for subsequent use as SRMs.

2.3. Evaluation of neuregulin-1-loaded sustained-release microspheres

2.3.1. Particle size distribution

The particle size distribution of NRG1-SRMs was measured using a laser diffraction particle size analyzer (LS-909, OMEC Instruments, China). Approximately 10 mg of dried microspheres were dispersed and analyzed in a quartz cuvette.

2.3.2. Encapsulation efficiency

To assess encapsulation efficiency, 10 mg of microspheres were dissolved in 10 mL of dichloromethane and centrifuged at 10,000 rpm for 5 min. The supernatant containing PLGA was discarded, and the NRG1-loaded core was resuspended in phosphate-buffered saline (PBS). The concentration of NRG1 was quantified using an enzyme-linked immunosorbent assay (ELISA) kit (RDR-NRG1-Ra-96T, Reddot Biotech, Canada). Encapsulation efficiency was calculated using the following formula:

$$\text{Encapsulation efficiency (\%)} = (Wa/Wt) \times 100 \quad \text{(I)}$$

where *Wa* is the actual weight of NRG1, and *Wt* is the theoretical loading. Each experiment was repeated five times.

2.3.3. In vitro release of neuregulin-1-loaded sustained-release microspheres

For *in vitro* release studies, 10 mg of NRG1-SRMs were suspended in 1 mL of PBS and incubated at 37°C under continuous agitation. At 2-day intervals, the entire volume of PBS was collected and replaced with an equal volume of fresh buffer. The concentration of NRG1 in the collected supernatants was quantified using an ELISA kit (KL-NRG1-Mu, KALANG, China). Each experiment was performed in quintuplicate.

2.3.4. Preparation of three dimensional-printed neuregulin-1 microsphere hydrogel scaffolds

To fabricate the 3D scaffolds, NRG1-SRMs were mixed with 20% gelatin and 4% sodium alginate at a volume ratio of 2:1:1 and maintained at 37°C. The resulting mixture was loaded into a 1 mL syringe equipped with a 100 μm nozzle. Extrusion and scanning speeds were set at 0.1 mL/s and 2.5 mm/s, respectively. The printing process was conducted at 25°C to generate cylindrical, grid-like scaffolds. Following fabrication, the scaffolds were immersed in 10% (w/v) calcium chloride at 5°C for 5 min to induce crosslinking. The excess solution was removed, and the scaffolds were rinsed thoroughly and stored in sterile PBS for subsequent use.

2.3.5. Cell compatibility evaluation

For cell viability testing, cells were embedded directly within the hydrogel scaffold by mixing at a density of 1×10^6 cells/mL prior to 3D printing. The cell–hydrogel mixture was then printed to fabricate cell-laden scaffolds. Cell viability within the scaffold was assessed using the Live/Dead cell imaging kit (R37601, Invitrogen, Thermo Fisher Scientific, USA). The 3D-printed scaffold was incubated in calcein AM (2 μM) and propidium iodide (PI; 8 μM) at 20–25°C for 15 min and examined under a laser scanning microscope (LSM880 with Fast Airyscan; ZEISS, Germany). The results were analyzed using Image-Pro Plus (IPP) 6.0 software (Media Cybernetic Inc., USA).

2.3.6. Scanning electron microscopy

Samples were fixed in glutaraldehyde for 6 h, followed by dehydration through a graded ethanol series. Subsequently, the samples were immersed in acetone for 15 min to

eliminate residual ethanol and then transferred to isoamyl acetate for 15 min to replace the acetone. Critical point drying was performed for 4 h using a Hitachi apparatus (Japan). The dried specimens were then sputter-coated with gold and examined using a Quanta 200 scanning electron microscope (FEI, USA).

2.4. Cell culture

2.4.1. Acquisition, culture, and neuregulin-1-loaded sustained-release microsphere treatment of bone marrow-derived Schwann-like cells

To isolate B-dSCs, femurs from neonatal rats were harvested under sterile conditions and flushed 15–20 times with α-minimum essential medium (α-MEM; Gibco, USA) containing 10% fetal bovine serum (FBS; Gibco, USA) and penicillin/streptomycin (50 U/mL and 50 mg/mL, respectively). The cell suspension was filtered through a 200-mesh sieve and cultured at 37°C. After 12 h, the medium was refreshed to remove non-adherent cells. Thereafter, media were changed every 3–4 days.

Third-passage BMSCs were induced to differentiate into Schwann-like cells using a stepwise protocol. Cells were suspended at 1×10^5 cells/mL in a mixed induction medium (1:1 Dulbecco's modified eagle medium [DMEM]/F12 and neurobasal medium) supplemented with basic fibroblast growth factor (bFGF; 40 ng/mL), epidermal growth factor (20 ng/mL), and B27 (2%). Neurospheres formed after 3 weeks were transferred to poly-L-lysine-coated flasks and cultured in basal medium supplemented with 10% FBS, forskolin (5 mM), platelet-derived growth factor with two A subunits (5 ng/mL), bFGF (10 ng/mL), and β-heregulin (200 ng/mL). The resulting B-dSCs were further cultured in DMEM/F12 with 10% FBS. Cells were seeded with NRG1-SRMs (1×10^5 cells per well) in 12-well plates, and the medium was replaced after 36 h. Successful differentiation of BMSCs into Schwann-like cells (B-dSCs) was confirmed by immunofluorescence staining for Schwann cell-specific markers S-100 and glial fibrillary acidic protein (GFAP) (Figure A1A and A1B). Additionally, the efficacy of this differentiation protocol was verified in our previously published study.[7]

2.4.2. Acquisition, culture, and neuregulin-1-loaded sustained-release microsphere treatment of autologous Schwann cells

To isolate ASCs, 0.5 cm segments of the radial nerve were excised and enzymatically digested with 0.05% collagenase. The digested tissue was triturated and filtered. Cells were cultured in DMEM/F12 with 10% FBS in a humidified 10% carbon dioxide incubator. Fibroblasts were removed using cytosine arabinoside and G418. bFGF was added to promote Schwann cell proliferation. Schwann cells were identified by vimentin staining. For treatment, 1×10^5 ASCs were co-incubated with NRG1-SRMs in 12-well plates, and the medium was replaced after 36 h.

2.4.3. Targeted inhibition of c-Jun N-terminal kinase pathway in bone marrow-derived Schwann-like cells

B-dSCs (1×10^5/mL) were seeded in 24-well plates and cultured for 24 h at 37°C. Cells were then treated with SP600125 (a JNK inhibitor; Sigma, USA) in complete medium. Lysates were collected using radioimmunoprecipitation assay (RIPA) buffer containing sodium dodecyl sulfate (SDS) and protease inhibitors. Protein concentrations were measured by Bradford assay, and JNK phosphorylation was assessed by Western blotting to confirm pathway inhibition.

2.4.4. Construction of bone marrow-derived Schwann-like cells/Schwann cells–dorsal root ganglion co-culture model

Dorsal root ganglia (DRG) were harvested from an 8-week-old Sprague–Dawley rat. DRG neurons were seeded onto 12 × 12 mm square glass coverslips pre-coated with 0.2% poly-L-lysine (P875130-25mg, Macklin, China) and placed in six-well culture plates. The neurons were maintained in neurobasal medium supplemented with B27, 0.08% glucose, nerve growth factor (NGF; 50 ng/mL), and 5-fluorodeoxyuridine (15 μM; Sigma-Aldrich, USA) to inhibit the proliferation of non-neuronal cells. Once DRG axons extended to the edges of the coverslips, Schwann cells were seeded at a density of 1.5×10^5 cells per coverslip and cultured in MEM supplemented with 10% FBS, 0.08% glucose, and 50 ng/mL NGF. After 7 days, the culture medium was switched to a myelination-inducing medium containing MEM, 10% FBS, 0.08% glucose, 50 ng/mL NGF, and 50 μg/mL ascorbic acid.

2.5. Evaluation of cell morphology and migration ability

2.5.1. Immunofluorescence staining

Cells were fixed with cold methanol for 25 min, blocked with 5% normal goat serum and 0.3% Triton X-100, and incubated overnight with S-100 antibody (1:800; Sigma, USA). After PBS washes, cells were incubated with an Alexa Fluor 492-conjugated secondary antibody (1:100; Servicebio, China) and counterstained with 4',6-diamidino-2-phenylindole (DAPI). Samples were mounted and visualized using a Nikon E800 fluorescence microscope.

2.5.2. Observation of cell morphology under a light microscope

Cell morphology was observed and recorded 24h after seeding using a Nikon E800 microscope.

2.5.3. Scratch assay

A sterile 10μL pipette tip was used to create a linear scratch across confluent cell monolayers in 24-well plates. After washing with PBS to remove cellular debris, fresh culture medium was added. Images were captured at 0 and 48h post-scratch. The initial scratch width was consistently maintained at approximately 500μm across all groups to ensure experimental comparability. The wound closure area was quantified using IPP software (Media Cybernetic Inc., USA), and the cell migration rate was calculated accordingly.

2.5.4. Transwell migration assay

Migration was assessed using BD BioCoat inserts (6.5mm diameter, 8μm pore size). Cells (1.5×10^5 per well) were seeded into the upper chamber with medium, and complete medium containing uridine triphosphate was added to the lower chamber as a chemoattractant. After 24h, migrated cells were fixed with ethanol, stained with crystal violet, and counted under a light microscope.

2.6. Evaluation of the dorsal root ganglion–Schwann cells/bone marrow-derived Schwann-like cells co-culture system

2.6.1. Immunofluorescence staining

Samples were permeabilized, blocked, and sequentially incubated with myelin basic protein (MBP; 1:800; Abcam, UK) and neurofilament heavy (NF200; 1:2000; Sigma, USA) primary antibodies. After washing, secondary antibodies (Alexa Fluor 594 and 488) were applied. Nuclei were counterstained with DAPI. Images were captured using a Nikon E800 microscope.

2.6.2. Western blot

Protein lysates were prepared from co-culture systems using RIPA buffer. After SDS-polyacrylamide gel electrophoresis and membrane transfer, blots were blocked and incubated overnight with primary antibodies against early growth response protein 2 (Krox-20; 1:1000; Abcam, UK), myelin-associated glycoprotein (MAG; 1:1000; GB11260-100, Servicebio, China), neurotrophin receptor (p75; 1:1400; GB115462-100, Servicebio, China), GFAP (1:1500; GB15100-100, Servicebio, China), glial-derived neurotrophic factor (GDNF; 1:1200; GB11403-100, Servicebio, China), phosphorylated JNK (1:300; GB15018-100, Servicebio, China), and JNK (1:1000; GB114321-100, Servicebio, China). Horseradish peroxidase-conjugated secondary antibodies (1:1000; Sigma, USA) were applied, and signals were detected using enhanced chemiluminescence. Quantification was performed using ImageJ (National Institutes of Health, USA).

2.7. Construction of peripheral nerve injury rat model and *in vivo* evaluation

2.7.1. Construction of peripheral nerve injury rat model

Rats were anesthetized with atropine (15mg/kg) and xylazine (1mg/kg), followed by 3% isoflurane. A 1cm segment of the sciatic nerve was resected and bridged using silicone tubes (length: 1.2cm; inner diameter: 2mm; wall thickness: 0.2mm; see Figure 5B) containing different scaffold compositions: PBS, NRG1-SRMs, B-dSCs, or both. Sham-operated animals received skin incisions without nerve transection. In groups involving cell transplantation, cells were embedded within the 3D-printed hydrogel scaffolds prior to implantation. Each group comprised six rats.

2.7.2. In vivo neuregulin-1 release and hydrogel scaffold degradation assessment

Scaffolds were implanted subcutaneously, and tissue samples were collected on days 1, 3, 7, 14, and 28. NRG1 expression was assessed by immunofluorescence using a rabbit anti-NRG1 primary antibody (1:200; Abcam, UK) followed by Alexa Fluor 594-conjugated secondary antibody (1:500). NRG1 itself does not exhibit autofluorescence. Three rats per group per time point were used for analysis. The fluorescent signal intensity of NRG1 was quantified using integrated optical density (OD) measurements to generate release curves.

To evaluate the structural integrity and degradation profile of the 3D-printed hydrogel scaffold *in vivo*, scaffolds were subcutaneously implanted in rats and harvested at 10, 20, and 30 days post-implantation. Due to the high water content and fragile structure of the hydrogel, conventional paraffin or cryosection embedding was not feasible. Instead, the explanted scaffolds were gently rinsed in PBS and embedded in 2% agarose at room temperature. The embedded samples were sectioned into 100 μm-thick slices using a vibrating microtome (Leica VT1000S, Germany). Sections were stained with hematoxylin and eosin (H&E) to visualize internal scaffold morphology and degradation over time.

2.7.3. Green fluorescent protein tracing of bone marrow-derived Schwann-like cells

Green fluorescent protein (GFP)-labeled B-dSCs were implanted within the scaffolds. Tissue sections were collected on day 3 for p75 immunostaining and on week 4 for MBP immunostaining. Fluorescence images were acquired using a Nikon fluorescence microscope and analyzed using ImageJ software.

2.7.4. Immunofluorescence staining

Fresh nerve graft specimens were harvested and cryosectioned at a thickness of 5–10μm. Tissue sections were incubated overnight at 4°C with primary antibodies against NF200 (1:2000; Sigma-Aldrich, USA) and MBP (1:800; Abcam, UK). Following PBS washes, Alexa Fluor 488- and 594-conjugated secondary antibodies were applied for 1h at room temperature. Fluorescence images were acquired using a Nikon fluorescence microscope (Digital Sight US-U2, Japan) equipped with a high-resolution digital camera. Quantitative analysis was performed using IPP software (Media Cybernetics Inc., USA).

2.7.5. Transmission electron microscopy

A 4-week observation period was selected to assess early-stage nerve regeneration and myelin sheath formation. Previous studies have indicated that early remyelination and initial axonal regeneration can be effectively evaluated at this stage.[7] Future studies with longer observation periods will further evaluate complete functional recovery. Nerve grafts were collected at 4 weeks post-surgery. After removal of surrounding adipose and vascular tissues, nerves were fixed in 2.5% glutaraldehyde at 4°C for 6h and washed in PBS (pH 7.2). Samples were then post-fixed in 1% osmium tetroxide, dehydrated through a graded acetone series, and embedded in Poly/Bed 812 resin (Ted Pella, USA). Polymerization was carried out at 60°C for 48h. Ultrathin sections (60–80nm) were cut using a Leica EM UC7 ultramicrotome and mounted onto 200-mesh formvar-coated copper grids. Sections were stained with uranyl acetate and lead citrate and then examined using a FEI Tecnai Spirit G2 Transmission Electron Microscope (TEM).

Six TEM sections and six toluidine blue-stained sections were prepared per group. Myelin thickness, axon diameter, the number of myelinated fibers, and the G-ratio[40] (**Equation II**; axon diameter divided by fiber diameter) were calculated using IPP software.

$$\text{G-ratio} = AD/(AD+MT) \quad \text{(II)}$$

where AD is axon diameter, and MT is myelin sheath thickness. All G-ratio assessments were performed by a pathologist blinded to the experimental groups.

2.7.6. Muscle wet weight and histological analysis

Following euthanasia, bilateral gastrocnemius muscles were harvested, and wet weights were measured using a precision electronic scale. The relative muscle weight was calculated as:

$$\text{Relative weight (\%)} = (\text{experimental side/control side}) \times 100 \quad \text{(III)}$$

Muscle tissues were fixed in 4% paraformaldehyde overnight, dehydrated, and embedded in paraffin. Cross-sections (5μm) were prepared and stained with Masson's trichrome. Muscle fiber morphology and area were visualized using a Nikon fluorescence microscope (Digital Sight US-U2, Nikon, Japan).

2.7.7. Neuromuscular junction synapse fluorescence staining

Frozen transverse sections (5–10μm) of the mid-belly gastrocnemius were prepared. Sections were incubated overnight at 4°C with primary antibodies against NF200 (1:1000; Servicebio, China) and synaptophysin (1:1000; Servicebio, China). After PBS washes, Alexa Fluor 594- and 488-conjugated secondary antibodies were applied at room temperature for 2h. Following final washes, images were acquired using a Nikon fluorescence microscope and quantified using IPP software.

2.7.8. Sciatic nerve functional index

Three rats from each group were randomly selected, and gait parameters were recorded at week 0, 1, 2, 3, and 4 post-surgery. Measurements included experimental paw length (EPL), toe spread (ETS), and intermediary toe spread (EIT), along with the corresponding values for the contralateral side (NPL, NTS, NIT). The sciatic nerve functional index (SFI) was calculated using the formula:

$$\text{SFI} = -38.3*(\text{EPL} - \text{NPL})/\text{NPL} + 109.5 \times (\text{ETS} - \text{NTS})/\text{NTS} + 13.3 \times (\text{EIT} - \text{NIT})/\text{NIT} - 8.8 \quad \text{(IV)}$$

2.7.9. Electrophysiological testing

At 4 weeks post-surgery, electrophysiological recordings were conducted using an RM6240 multi-channel signal acquisition system (Chengdu Instrument Factory, China). Under pentobarbital anesthesia (45mg/kg), the sciatic nerve graft site was re-exposed. A stimulating electrode was placed 0.5cm proximal to the graft site, and a recording electrode was inserted into the triceps surae muscle. Stimulation parameters were: 1–2 mA current, 0.1 ms pulse duration, and 1.0 Hz frequency. Compound muscle action potential amplitude (AP), latency (LT), and conduction velocity (CV) were recorded and analyzed.

2.7.10. Magnetic resonance imaging

At 4 weeks post-surgery, rats were anesthetized and scanned using a Bruker PharmaScan 70/16 Ultra-Shielded Magnetic Resonance Imaging (MRI) system (Germany). High-resolution T2-weighted sagittal images

were acquired, focusing on the sciatic nerve region. Signal intensity and structural continuity at the injury site were evaluated to assess nerve regeneration.

2.7.11. Statistical analysis

Data are presented as mean ± standard deviation. Statistical comparisons between groups were performed using one-way analysis of variance (ANOVA) followed by Tukey's multiple comparison test. A significance threshold of $\alpha = 0.05$ was applied. All statistical analyses were conducted using GraphPad Prism 9.0 software (GraphPad Software, USA).

3. Results

3.1. Characterization and evaluation of three-dimensional-printed hydrogel scaffolds with neuregulin-1 sustained-release microspheres

3.1.1. Morphological characterization, encapsulation efficiency (neuregulin-1 ELISA kit), particle size distribution, and in vitro release profile

(a) **Particle size distribution of NRG1-loaded SRMs** Scanning electron microscopy revealed that NRG1-SRMs were spherical with slightly rough surface textures and displayed good dispersion without noticeable aggregation (Figure 1A-a1). The microspheres demonstrated a relatively uniform size distribution, with an average diameter of 19.4 ± 4.3μm (Figure 1A-a1 and 1C).

(b) **Morphological evaluation of 3D-printed hydrogel** *scaffolds*Using sodium alginate as the primary component, we successfully fabricated multilayered, grid-like 3D-printed scaffolds (Figure 1B). SEM analysis revealed scaffold fibers with an average diameter of approximately 80 μm and an interconnected porous architecture with pore sizes around 120 μm (Figure 1A-a4). The NRG1-SRMs were uniformly distributed across the scaffold surface (Figure 1A-a2 and 1A-a3), appearing as hemispherical protrusions (~20μm in diameter), without compromising scaffold structural integrity.

(c) **Encapsulation efficiency of NRG1-loaded SRMs** Encapsulation efficiency, determined using an NRG1 ELISA kit, was 84 ± 4.3% (w/w).

(d) **In vitro release profile of NRG1-loaded SRM** Enzyme-linked immunosorbent assay-based analysis demonstrated continuous NRG1 release over 30 days. On day 30, cumulative release from the 3D-printed hydrogel scaffolds reached 88.7 ± 1.2%, compared to 36.3 ± 1.2% from non-printed hydrogels (Figure 1D).

3.1.2. Cell compatibility test

Live/dead staining showed a significantly higher cell survival rate in 3D-printed scaffolds (87.2 ± 1.3%) compared to non-printed hydrogels (73.8 ± 3.7%) (Figure 1F), confirming the scaffold system's excellent cytocompatibility.

3.1.3. In vivo release of NRG1-loaded sustained-release microspheres

3D-printed scaffolds were implanted subcutaneously, and NRG1 fluorescence was assessed on days 0, 3, 7, 14, 21, and 28 (n=3). Fluorescence intensity gradually decreased over time, with a relative OD of 0.77 ± 0.05 on day 3 and 0.26 ± 0.03 on day 28 (Figure 1G and H), indicating sustained *in vivo* release.

3.1.4. Distribution of neuregulin-1-loaded sustained-release microspheres in non-printed and three-dimensional-printed hydrogels

In non-printed hydrogels, microspheres showed sedimentation, with significantly higher density in the lower layer (15.0 ± 2.5/18,000μm^2) compared to the upper layer (4.4 ± 1.1/18,000μm^2; $p < 0.01$). In contrast, 3D-printed scaffolds demonstrated uniform distribution across both layers (upper: 16.8 ± 2.6; lower: 16.0 ± 2.8) (Figure 1I and J).

3.2. Dorsal root ganglion and autologous Schwann cells/bone marrow-derived Schwann-like cells co-culture

NRG1 significantly enhanced the myelination ability of B-dSCs in a DRG co-culture system. This effect is mediated via the JNK signaling pathway, as shown by increased myelin-associated protein expression, which is reversed upon JNK inhibition.

3.2.1. Quantification of neurofilament length and myelination via immunofluorescence staining

To assess neurofilament outgrowth and myelination, five DRG neurons were randomly selected from each co-culture group for analysis (Figure 2A, green; Table 1). Fluorescence co-localization analysis revealed a strong spatial overlap between MBP and NF200 in the N+B group, indicating enhanced myelination of B-dSCs upon NRG1 treatment (Figure 2B).

Quantification of neurite extension length (Figure 2C) showed that both the N+A group (202.60 ± 8.55μm) and N+B group (202.60 ± 7.94μm) had significantly longer neurites than the ASC group (157.60 ± 6.80μm) and B-dSC group (45.00 ± 6.23μm) ($p < 0.05$).

For myelination analysis, five immunofluorescence images per group were used to quantify MBP fluorescence intensity (Figure 2A, red; Figure 2D). The N+A (1.06 ± 0.19) and N+B (1.00 ± 0.26) groups showed

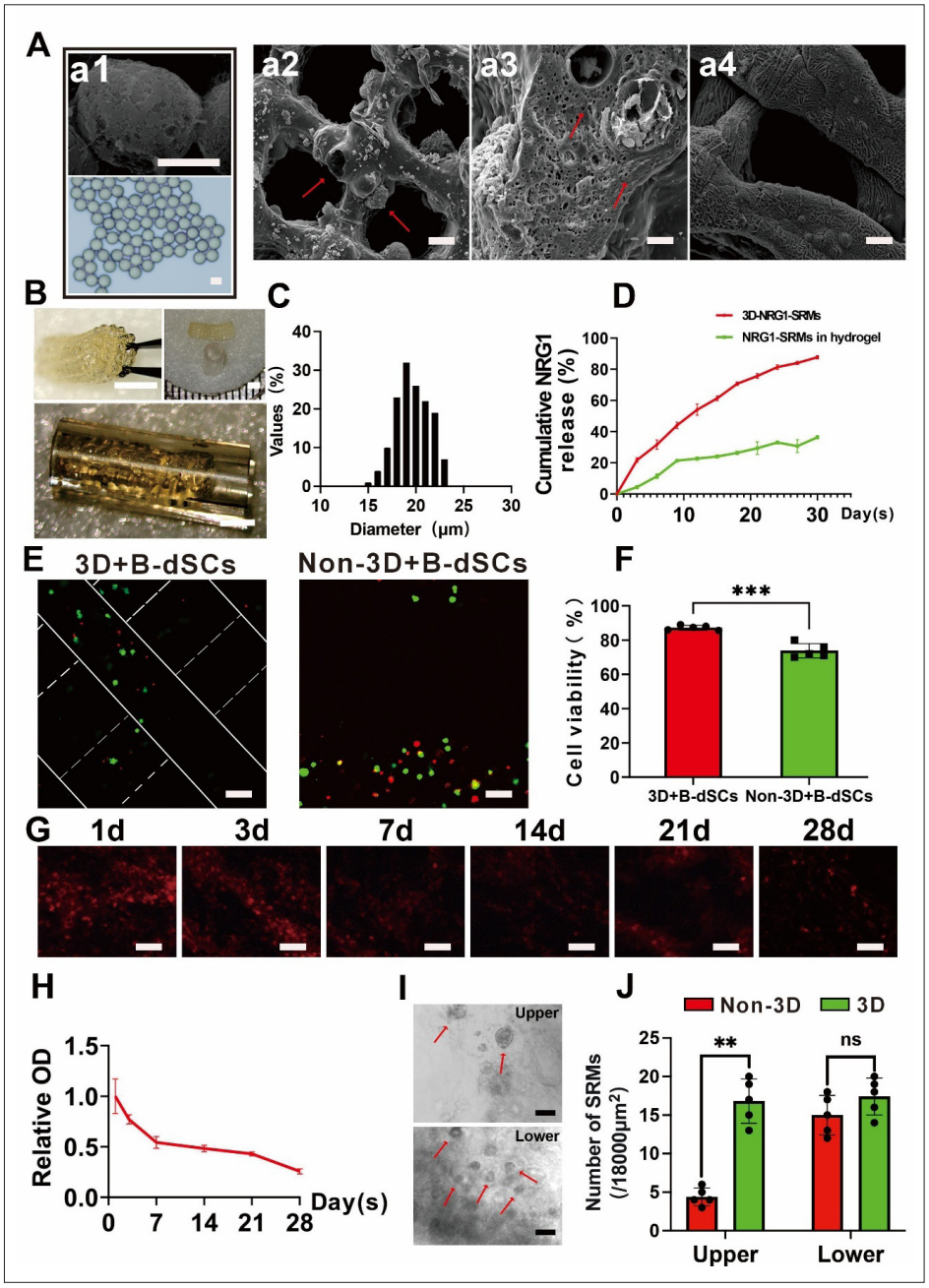

Figure 1. Preparation and characterization of three-dimensional-printed hydrogel scaffolds with neuregulin-1 sustained-release microspheres (3D-NRG1-SRMs). (A) Scanning electron microscopy and microscopic images showing the morphology of (a1) NRG1-SRMs, (a2, a3) 3D-NRG1-SRMs, and (a4) 3D-printed hydrogel scaffolds without NRG1-SRMs. Red arrows indicate the NRG1-SRMs in the scaffold. (B) Photographs showing the 3D-printed hydrogel scaffold before implantation. The scaffold was inserted into a silicone tube (inner diameter: 2.5 mm), demonstrating dimensional compatibility. The scaffold diameter was approximately 2 mm and its length 10 mm, allowing tight yet feasible insertion into the conduit. (C) Particle size distribution of NRG1-SRMs, showing an average diameter of 19.4 ± 4.3 μm. (D) In vitro release profiles of NRG1-SRMs in 3D-printed and non-3D printed hydrogels, demonstrating sustained NRG1 release over 30 days. (E) Live/dead staining of bone marrow-derived Schwann-like cells (B-dSCs) in 3D-printed and non-3D-printed hydrogels. (F) Quantification of the proportion of live cells in (E), indicating higher cell viability in 3D-printed hydrogels. (G) Subcutaneous NRG1 fluorescence staining over 28 days, illustrating the gradual release of NRG1 from the microspheres. (H) Quantitative analysis of NRG1 release from 3D-NRG1-SRMs in vivo. (I) Light microscopy images comparing the distribution of NRG1-SRMs in the upper and lower layers of non-3D printed hydrogels. Red arrows indicate the NRG1-SRMs in the hydrogel. (J) Quantification of NRG1-SRMs distribution in 3D-printed and non-3D-printed hydrogels, showing more uniform distribution in 3D-printed hydrogels. Statistical significance was determined using non-parametric t-tests. Scale bars: a1 = 10 μm; a2 and a4 = 30 μm; a3 = 15 μm; B = 2 mm; E and G = 50 μm; I = 30 μm. Magnifications: a1 = 2500×; a2 and a4 = 1000×; a3 = 1500×; B = 1×; E and G = 100×; I = 400×.

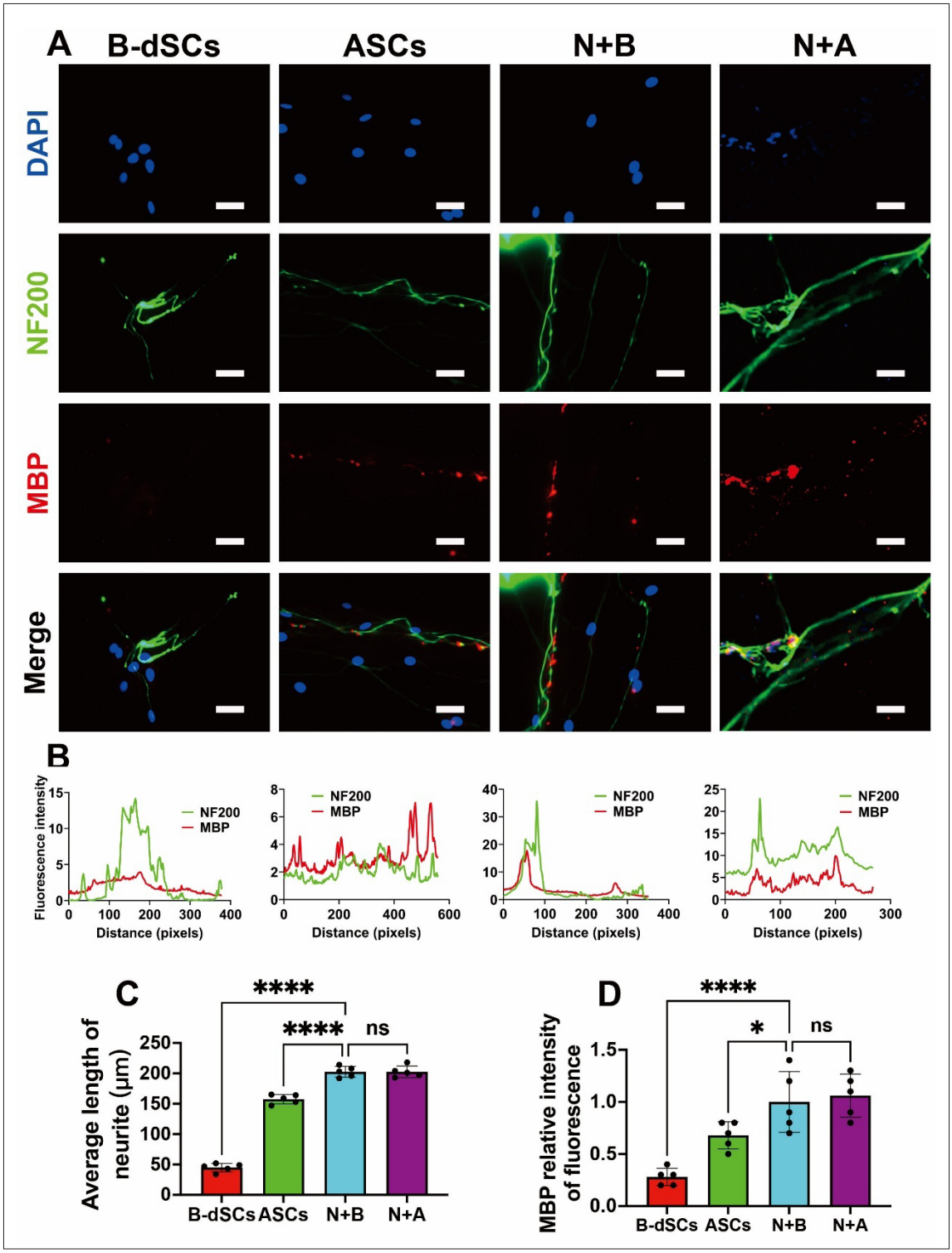

Figure 2. Immunofluorescence analysis of B-dSC/ASC and DRG neuron co-culture. (A) Co-staining of axons (NF200, green) and myelin sheaths (MBP, red) in the co-culture system. (B) Immunofluorescence co-localization of NF200 and MBP, showing poor co-localization in the B-dSCs group. (C) Quantification of axon length, revealing significantly longer neurites in the NRG1-treated groups. (D) Quantification of relative myelin expression, indicating higher MBP expression in the NRG1-treated groups. Statistical significance was determined using one-way analysis of variance with Tukey's post hoc test. $^{*}p < 0.05$, $^{****}p < 0.0001$, $^{ns}p > 0.05$. Scale bar = 40 μm; magnification = 400×. *Notes*: N+A: (NRG1 + ASCs) + DRG co-culture; N+B: (NRG1 + B-dSCs) + DRG co-culture. Abbreviations: ASC, autologous Schwann cell; B-dSC, bone marrow-derived Schwann-like cell; DRG, dorsal root ganglion; MBP, myelin basic protein; NF200, neurofilament heavy; NRG1, neuregulin-1.

Table 1. Co-culture groups and corresponding treatment methods

Group (n=3)	Treatment method
(1) B-dSCs	B-dSCs + DRG co-culture
(2) ASCs	ASCs + DRG co-culture
(3) N+B	(NRG1 + B-dSCs) + DRG co-culture
(4) N+A	(NRG1 + ASCs) + DRG co-culture
(5) N+B+I	(SP600125 + NRG1+B-dSCs) + DRG co-culture

Abbreviations: ASCs, autologous Schwann cells; B-dSC, bone marrow-derived Schwann-like cells; DRG, dorsal root ganglion; NRG1, neuregulin-1.

markedly higher MBP levels than the ASC (0.68 ± 0.12) and B-dSC (0.28 ± 0.07) groups ($p < 0.05$).

3.2.2. Western blot analysis of myelin-related transcription factors and protein expression

Western blot analysis was conducted to assess the expression of key transcription factors and myelin-associated proteins in the DRG co-culture system. The relative expression of Krox-20, a pivotal transcription factor for myelin formation, was significantly upregulated in the N+B group (1.41 ± 0.11) compared to the ASC (1.05 ± 0.04) and B-dSC (0.91 ± 0.15) groups but remained lower than in the N+A group (1.81 ± 0.05) (Figure 3A).

Similarly, the expression of the MAG followed the same trend. The N+B group exhibited a relative MAG expression level of 1.55 ± 0.07, which was higher than that observed in the ASCs group (1.09 ± 0.05) and the B-dSCs group (0.88 ± 0.03), but slightly lower than in the N+A group (1.64 ± 0.26) (Figure 3C and D).

These results indicate that treatment with NRG1 significantly enhances the myelination potential of B-dSCs, though the response remains somewhat inferior to that of native ASCs under the same conditions. Nonetheless, the NRG1-induced improvement in B-dSC function highlights its potential for regenerative applications in PNI.

3.2.3. Validation of c-Jun N-terminal kinase pathway inhibition in the dorsal root ganglion–bone marrow-derived Schwann-like cell co-culture system

To verify whether the JNK signaling pathway mediates the effects of NRG1 on B-dSC dedifferentiation and myelination, we introduced SP600125, a selective JNK inhibitor, into the DRG–B-dSCs co-culture system treated with NRG1-SRMs (Figure 3B). Western blot analysis showed that the expression of phosphorylated JNK in the inhibitor group (NRG1 + SP600125 + B-dSCs) was significantly decreased compared to the NRG1 + B-dSCs group (Figure 3E and F), confirming effective suppression of the JNK pathway.

Subsequently, we assessed downstream functional markers. In the presence of SP600125, the protein expression levels of Krox-20 (0.71 ± 0.06), p75 (0.72 ± 0.03), MAG (0.90 ± 0.11), GFAP (0.86 ± 0.05), and GDNF (0.85 ± 0.03) were significantly reduced compared to the NRG1 + B-dSCs group (Krox-20: 1.41 ± 0.11; p75: 1.18 ± 0.04; MAG: 1.55 ± 0.07; GFAP: 1.35 ± 0.02; GDNF: 1.49 ± 0.03), all $p < 0.05$.

These findings suggest that NRG1 enhances B-dSCs dedifferentiation and myelination, in part through activation of the JNK signaling pathway. Inhibition of JNK reverses these effects, indicating its essential regulatory role in NRG1-mediated functional enhancement of B-dSCs.

3.3. Comparison of Schwann cell and bone marrow-derived Schwann-like cell morphology and migration ability before and after neuregulin-1 induction

To further characterize the effects of NRG1 on B-dSC function, we evaluated their morphological features and migratory capacity under both two-dimensional (2D) and 3D conditions. These experiments revealed that NRG1 significantly promotes morphological maturation and enhances motility of B-dSCs, thereby improving their functional resemblance to native Schwann cells.

3.3.1. Morphological changes in Schwann cells and bone marrow-derived Schwann-like cells before and after neuregulin-1 induction

At 24 h post-seeding, all cells adhered well to the culture surface. Microscopic examination revealed distinct morphological differences among the groups (Table 2). In the N+B group, 72.1 ± 3.1% of cells exhibited a bipolar or multipolar spindle-shaped morphology, comparable to the N+A group (76.9 ± 2.5%). These proportions were significantly higher than those observed in the untreated B-dSC group (20.4 ± 3.0%) and the ASC group (34.1 ± 3.6%) (Figure 4A and D). These findings indicate that NRG1 stimulation induces a morphological transition in B-dSCs toward a Schwann cell-like phenotype, supporting their enhanced structural maturation.

3.3.2. Changes in Schwann cells and bone marrow-derived Schwann-like cell migration ability before and after neuregulin-1 induction under two-dimensional conditions (scratch assay)

To assess cell motility in a 2D environment, a scratch assay was performed. No significant differences were observed in initial scratch widths among groups, confirming consistent experimental conditions across all comparisons (initial scratch width ~500 μm). After 48 h, the migration rate in the N+B group reached 61.4 ± 3.2%, which was similar to that in the N+A group (72.8 ± 3.4%) and significantly

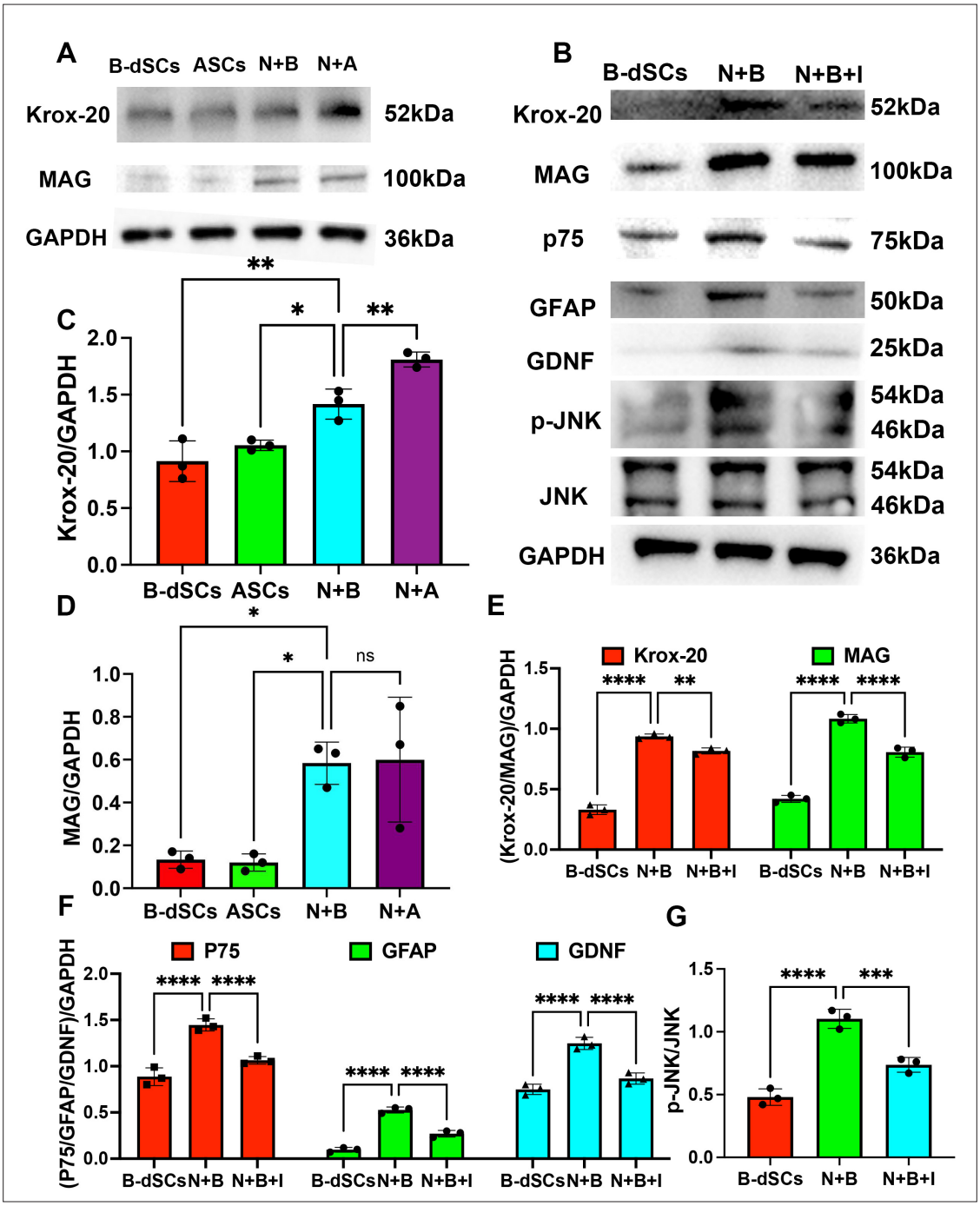

Figure 3. Western blot analysis of protein expression in the (B-dSC/ASC and DRG neuron co-culture system. (A) Western blot bands showing the expression of Krox-20 and MAG before and after NRG1 treatment in the co-culture system. (B) Western blot bands of myelin-related proteins (Krox-20, MAG), dedifferentiation markers (p75, GFAP, GDNF), and JNK pathway proteins (p-JNK, JNK) in the B-dSCs group, N+B group, and N+B+I group. (C, D) Quantification of Krox-20 and MAG expression levels before and after NRG1 treatment in the co-culture system. (E) Quantification of Krox-20 and MAG expression levels in B-dSCs, B-dSCs + NRG1 (N+B), and B-dSCs + NRG1 + SP600125 (N+B+I) co-cultured with DRG neurons. (F) Quantification of p75, GFAP, and GDNF expression in B-dSCs, B-dSCs + NRG1, and B-dSCs + NRG1 + SP600125 co-cultured with DRG neurons. (G) Quantification of p-JNK/JNK expression in B-dSCs, B-dSCs + NRG1 (N+B), and B-dSCs + NRG1 + SP600125 (N+B+I) co-cultured with DRG neurons. Statistical analysis was performed using one-way analysis of variance with Tukey's post hoc test. $^{*}p < 0.05$, $^{**}p < 0.01$, $^{***}p < 0.001$, $^{****}p < 0.0001$, $^{ns}p > 0.05$. Abbreviations: ASCs, autologous Schwann cells; B-dSCs, bone marrow-derived Schwann-like cells; GAPDH, glyceraldehyde 3-phosphate dehydrogenase; GDNF, glial-derived neurotrophic factor; GFAP, glial fibrillary acidic protein; JNK, C-Jun N-terminal kinase; Krox-20, early growth response protein 2; MAG, myelin-associated glycoprotein; NRG1, neuregulin-1; p75, neurotrophin receptor; p-JNK, phosphorylated JNK.

Table 2. *In vitro* cell culture groups and treatment methods

Group	Treatment method
(1) B-dSCs	B-dSCs treated with PBS
(2) ASCs	ASCs treated with PBS
(3) N+B	B-dSCs treated with NRG1
(4) N+A	ASCs treated with NRG1

Abbreviations: ASC, autologous Schwann cell; B-dSC, bone marrow-derived Schwann-like cell; NRG1, neuregulin-1; PBS, phosphate-buffered saline.

higher than in the B-dSC (31.6 ± 2.9%) and ASC (21.2 ± 2.8%) groups (Figure 4B and E). The migration rate was calculated using the formula:

$$\text{Migration (\%)} = (\text{Initial scratch width} - \text{Final scratch width})/\text{Initial scratch width} \times 100\% \quad \text{(V)}$$

These results indicate that NRG1 enhances the 2D migratory capacity of B-dSCs, comparable to native Schwann cells.

3.3.3. Changes in Schwann cells and bone marrow-derived Schwann-like cell migration ability before and after neuregulin-1 induction under three-dimensional conditions (transwell assay)

Cell migration was further evaluated under 3D conditions using a transwell assay. The relative number of cells that migrated through the membrane in the N+B group (1.0 ± 0.3) was similar to that in the N+A group (1.3 ± 0.2) and significantly higher than in the B-dSC (0.7 ± 0.1) and ASC (0.3 ± 0.1) groups (Figure 4C and F). These findings confirm that NRG1 promotes both 2D and 3D migratory capabilities in B-dSCs, aligning their behavior more closely with that of native Schwann cells.

3.4. Evaluation of *in vivo* gel scaffold degradation, myelin regeneration, and nerve function

Section 3.4 examines the sustained release behavior and biological activity of NRG1-SRMs. Results demonstrated that NRG1-SRMs released bioactive NRG1 in a controlled manner over 28 days, maintaining sufficient activity to support B-dSC viability and function. The grouping of animals used in the *in vivo* studies is summarized in Table 3.

3.4.1. In vivo fluorescence tracing of bone marrow-derived Schwann-like cells and gel scaffold degradation

To evaluate the *in vivo* fate and functional status of B-dSCs, we conducted fluorescence co-localization analysis at early and late stages post-transplantation (Figure 5A). GFP-labeled B-dSCs were found to co-express p75—a marker of early Schwann cell dedifferentiation—indicating successful phenotypic reversion in the repair microenvironment (Figure 5D). At later stages, GFP-positive cells also co-localized with MBP, a key myelin structural protein, suggesting that the transplanted B-dSCs not only survived *in vivo* but also contributed directly to remyelination (Figure 5D–F). *In vivo* degradation of the hydrogel scaffold (without NRG1-SRMs) was assessed by H&E staining of agarose-embedded sections collected at 10, 20, and 30 days after subcutaneous implantation. As shown in Figure 5B and C, the hydrogel exhibited a well-defined porous structure at day 10, which became progressively fragmented and less defined by days 20 and 30, indicating gradual degradation of the scaffold matrix. These results confirm the scaffold's ability to provide initial support while allowing for time-dependent resorption.

3.4.2. Immunofluorescence analysis of nerve and myelin regeneration

To quantify myelin regeneration, immunofluorescence staining for MBP was performed on sciatic nerve sections 4 weeks after injury. The relative MBP fluorescence intensity in the N+B group (0.80 ± 0.03) was comparable to that in the Sham group (1.00 ± 0.11), and significantly higher than in the PNI (0.11 ± 0.03), B-dSCs (0.51 ± 0.05), and NRG1-only (0.34 ± 0.05) groups ($p < 0.0001$) (Figure 6A and C). These findings confirm that combined treatment with NRG1 and B-dSCs yields superior myelin regeneration relative to either component alone.

3.4.3. Myelinated nerve fibers and large-diameter axons in regenerated nerves

The proportion of myelinated nerve fibers in the regenerated sciatic nerve was 71.3 ± 7.1% in the N+B group, closely approximating the Sham group (78.7 ± 4.1%), and significantly greater than in the PNI (14.3 ± 2.5%), B-dSCs (22.3 ± 2.5%), and NRG1 (35.7 ± 2.5%) groups ($p < 0.0001$) (Figure 6B and D).

Analysis of axon caliber revealed that the proportion of large-diameter axons (>2μm) in the N+B group (36.7 ± 1.5%) was slightly lower than that in the Sham group

Table 3. *In vivo* experimental groups and treatment methods

Group (*n*=6)	Treatment method
(1) PNI	PBS treatment
(2) NRG1	3D-NRG1-SRMs
(3) B-dSCs	3D scaffold (without NRG1-SRMs) + B-dSCs
(4) NRG1+B	3D-NRG1-SRMs + B-dSCs
(5) Sham	Sham operation

Abbreviations: B-dSCs, bone marrow-derived Schwann-like cells; NRG1-SRM, neuregulin-1-loaded sustained-release microspheres; PBS, phosphate-buffered saline; PNI, peripheral nerve injury; 3D, three-dimensional.

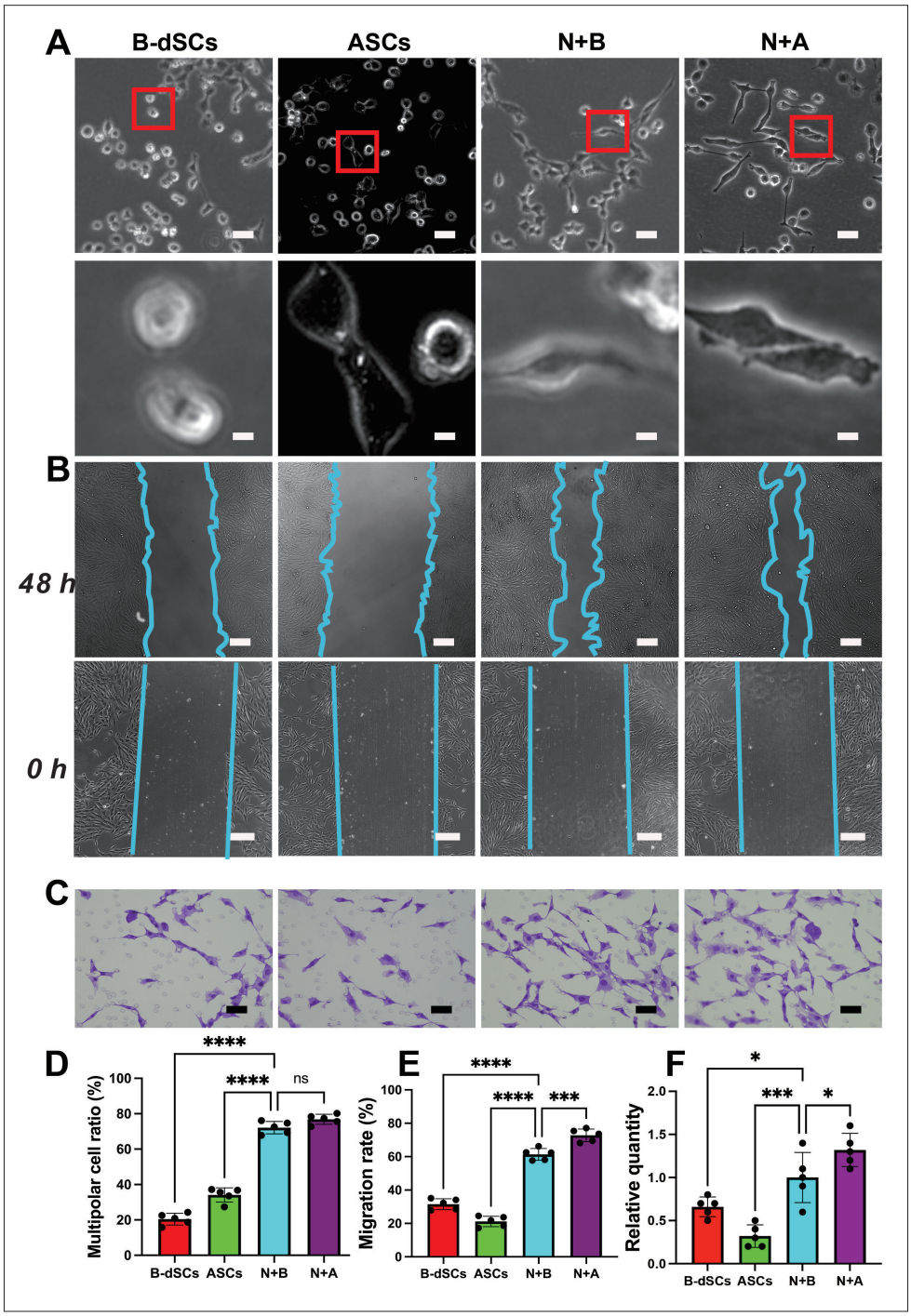

Figure 4. Morphology and motility of B-dSCs/ASCs before and after NRG1 treatment. (A) Light microscopy images of B-dSCs/ASCs before and after NRG1 treatment, including corresponding magnified views of the areas indicated by red boxes. (B) Two-dimensional motility of B-dSCs/ASCs assessed via scratch assay before and after NRG1 treatment. (C) Three-dimensional motility of B-dSCs/ASCs assessed via transwell assay before and after NRG1 treatment. (D) Quantification of the proportion of multipolar cells, demonstrating increased multipolarity following NRG1 treatment. (E) Quantification of cell migration rates in the scratch assay, showing enhanced migration in NRG1-treated groups. (F) Quantification of cell motility in the transwell assay, indicating increased motility in the NRG1-treated groups. Statistical analysis was performed using one-way analysis of variance with Tukey's post hoc test. $^{*}p < 0.05$, $^{***}p < 0.001$, $^{****}p < 0.0001$, $^{ns}p > 0.05$. Scale bars: (A upper) and (C) = 40 μm; (A lower) = 5 μm; (B upper) = 80 μm; (B lower) = 100 μm. Magnifications: (A upper) and (C) = 400×; (A lower) = 1000×; (B upper) = 40×; (B lower) = 100×. *Notes*: N+A: (NRG1 + ASCs) + DRG co-culture; N+B: (NRG1 + B-dSCs) + DRG co-culture. Abbreviations: ASC, autologous Schwann cell; B-dSC, bone marrow-derived Schwann-like cell; DRG, dorsal root ganglion; NRG1, neuregulin-1.

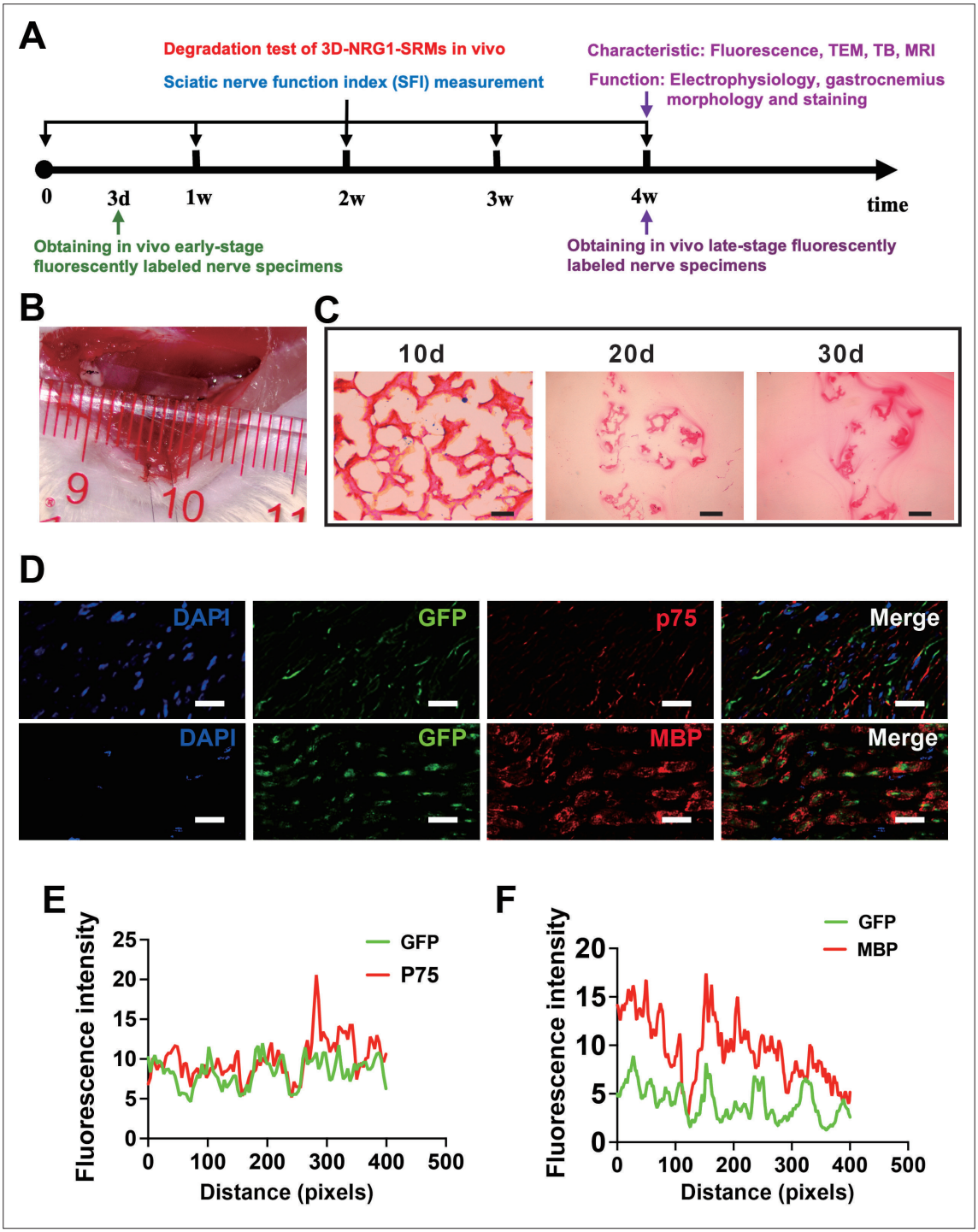

Figure 5. *In vivo* detection timeline and fluorescence tracing of bone marrow-derived Schwann-like cells (B-dSCs). (A) Schematic timeline for tissue collection and assessment following the establishment of peripheral nerve injury model. (B) Macroscopic intraoperative photograph showing the three-dimensional (3D)-printed hydrogel scaffold bridging the transected sciatic nerve ends within a silicone tube (inner diameter: 2.5 mm). A ruler is included for reference. (C) Hematoxylin and eosin staining of scaffold sections were collected from subcutaneous implantation sites at 10, 20, and 30 days (d), respectively. Progressive degradation of the porous hydrogel structure was observed over time. (D, E) Co-localization of GFP-labeled B-dSCs with p75 and MBP indicates their early dedifferentiation and subsequent myelination *in vivo*. Scale bars: (B) = 5 mm; (C) = 100 μm; (D) = 50 μm. Magnifications: (C) = 100×; (D) = 100×. Abbreviations: DAPI, 4',6-diamidino-2-phenylindole; GFP, green fluorescence protein; MBP, myelin basic protein; MRI, magnetic resonance imaging; NRG1-SRMs, neuregulin-1-loaded sustained-release microspheres; p75, neurotrophin receptor; TEM, transmission electron microscopy; TB, toluidine blue.

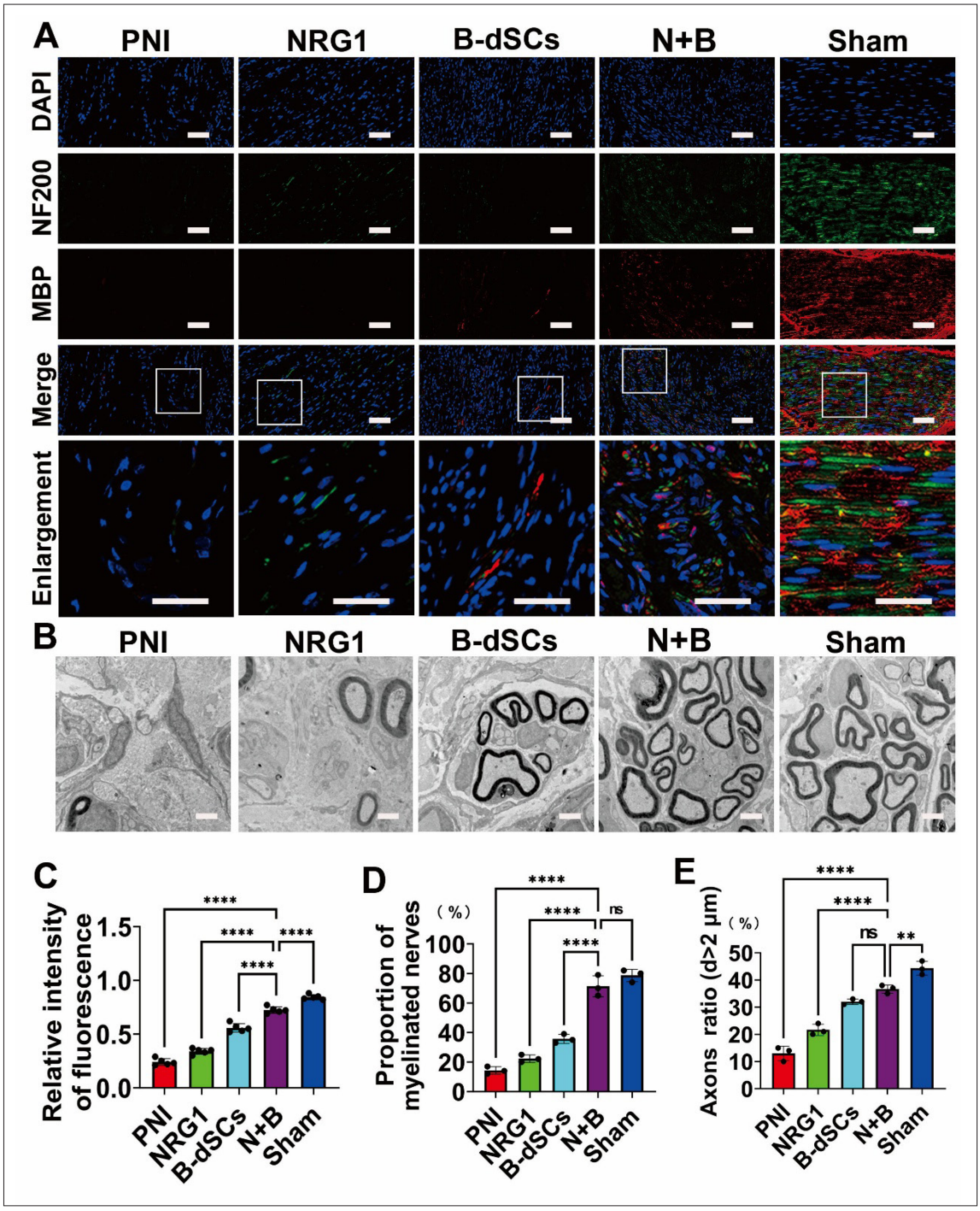

Figure 6. *In vivo* nerve regeneration and quantification of myelinated nerves and large-diameter axons. (A) Immunofluorescence staining of regenerated axons (NF200) and myelin sheaths (MBP) in sciatic nerve sections. (B) TEM images of nerve cross-sections at the distal end. (C) Quantification of relative MBP fluorescence intensity in (A), showing greater myelination in the N+B group. (D) Quantification of the proportion of myelinated nerve fibers in (A), indicating a higher proportion in the N+B group. (E) Quantification of the proportion of large-diameter axons (> 2 μm) in (A), showing enhanced axonal regeneration in the N+B group. Statistical analysis was performed using one-way analysis of variance with Tukey's post hoc test. $^{**}p < 0.01$, $^{***}p < 0.001$, $^{****}p < 0.0001$, $^{ns}p > 0.05$. Scale bars: (A) = 40 μm; (B) = 2 μm. Magnifications: (A) = 100×; (B) = 400×. *Note*: N+B: (NRG1 + B-dSCs) + dorsal root ganglion co-culture. Abbreviations: B-dSCs, bone marrow-derived Schwann-like cells; DAPI, 4',6-diamidino-2-phenylindole; MBP, myelin basic protein; NF200, neurofilament heavy; NRG1, neuregulin-1; PNI, peripheral nerve injury; TEM, transmission electron microscopy.

(44.3 ± 2.5%), but markedly higher than in the PNI (13.0 ± 2.6%), B-dSC (32.0 ± 2.1%), and NRG1 (21.7 ± 2.1%) groups (Figure 6B and E). These results indicate that combined NRG1 and B-dSC treatment not only promotes myelination but also supports axonal maturation and regeneration.

3.4.4. Myelin sheath thickness and G-ratio in regenerated nerves

TEM was employed to assess the structural maturity of regenerated myelin. The average myelin sheath thickness in the N+B group was 0.72 ± 0.03μm, which is slightly lower than that of the Sham group (0.84 ± 0.03μm), but significantly greater than in the PNI (0.23 ± 0.02μm), B-dSC (0.54 ± 0.03μm), and NRG1-only (0.33 ± 0.03μm) groups ($p < 0.001$) (Figure 7A and E). These results demonstrate that combined NRG1 and B-dSC treatment markedly enhances remyelination, achieving near-physiological myelin thickness.

The G-ratio (axon diameter/fiber diameter), a well-established indicator of myelin compactness, was analyzed separately for large- and small-diameter axons. For large-diameter axons (>2μm), the G-ratio in the N+B group (0.56 ± 0.05) approached the optimal physiological range (~0.6) and was comparable to that in the Sham group (0.67 ± 0.06). In contrast, the G-ratios in the B-dSCs (0.37 ± 0.05), NRG1-only (0.73 ± 0.04), and PNI (0.86 ± 0.06) groups deviated significantly from the ideal range (Figure 7B), indicating impaired remyelination or axonal degeneration.

For small-diameter axons, G-ratio values remained relatively consistent across all groups and aligned with the physiological norm: Sham (0.61 ± 0.09), N+B (0.59 ± 0.08), B-dSCs (0.59 ± 0.10), NRG1 (0.59 ± 0.09), and PNI (0.58 ± 0.07) (Figure 7C). Collectively, these findings suggest that NRG1-SRMs combined with B-dSCs not only enhance myelin thickness but also restore the structural integrity of large-caliber axons, thereby supporting improved functional recovery (Figure 7D and E).

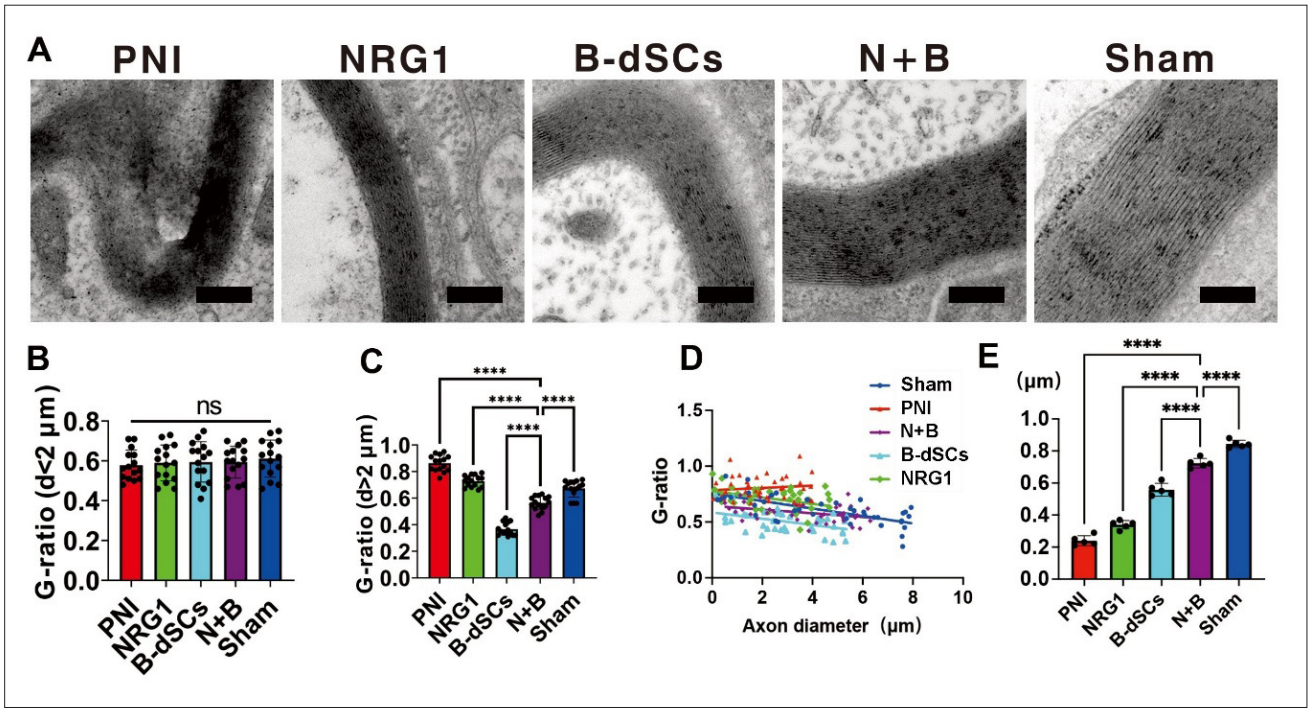

Figure 7. Myelin sheath thickness and G-ratio in regenerated nerves. (A) Transmission electron microscopy images of regenerated myelin sheaths, showing differences in thickness across groups. (B) Quantification of G-ratio for large-diameter axons (>2 μm), demonstrating optimal myelination in the N+B group. (C) Quantification of G-ratio for small-diameter axons (<2 μm), showing consistent ratios across all groups. (D) Scatter plot and fitted curves for the G-ratio in each group, highlighting the relationship between axon diameter and myelination. (E) Quantification of regenerated myelin sheath thickness, indicating significantly thicker myelin in the N+B group compared to others. $^{****}p < 0.0001$, $^{ns}p > 0.05$. One-way ANOVA with Tukey's post hoc test. Scale bar (A) = 200 nm; Magnification: (A) = 15,000×. *Note*: N+B: (NRG1 + B-dSCs) + dorsal root ganglion co-culture. Abbreviations: B-dSCs, bone marrow-derived Schwann-like cells; d, diameter; NRG1, neuregulin-1; PNI, peripheral nerve injury.

3.4.5. Gastrocnemius muscle wet weight and muscle fiber atrophy

At 4 weeks post-surgery, gastrocnemius muscles from both hindlimbs were harvested for wet weight measurement (Figure 8A). Relative muscle weight was calculated as:

$$\text{Relative weight (\%)} = (\text{Experimental side}/\text{Normal side}) \times 100 \quad \text{(VI)}$$

In the Sham group, no obvious difference was observed between the two limbs. In contrast, the injured muscle in the NRG1+B group was slightly reduced in size, while more severe atrophy was evident in the PNI, B-dSCs, and NRG1 groups. Quantitatively, the relative muscle weight in the N+B group (80.32 ± 3.48%) was significantly lower than in the Sham group (98.92 ± 0.37%) but notably higher than in the PNI (28.46 ± 1.32%), B-dSC (50.64 ± 4.33%), and NRG1 (51.08 ± 4.05%) groups ($p < 0.0001$) (Figure 8D).

Histological analysis using Masson's trichrome staining revealed the average cross-sectional area of muscle fibers (Figure 8B): Sham (1428.4 ± 42.81 μm^2), N+B (1205 ± 48.29 μm^2), B-dSCs (812.4 ± 36.21 μm^2), NRG1 (832.2 ± 54.55 μm^2), and PNI (539 ± 28.11 μm^2). Muscle atrophy in the N+B group was moderate and significantly improved compared to the other injury groups ($p < 0.0001$) (Figure 8E).

3.4.6. Neuromuscular junction synapse fluorescence staining

To evaluate neuromuscular reinnervation, immunofluorescence staining of neuromuscular junctions (NMJs) was performed on gastrocnemius muscle sections. The density of NMJs in the N+B group (29.6 ± 4.2 per 120,000 μm^2) was significantly lower than in the Sham group (50.4 ± 3.0), but markedly higher than in the PNI (2.6 ± 1.8), B-dSC (7.4 ± 3.0), and NRG1 (7.4 ± 1.1) groups (Figure 8C and F). These results indicate enhanced NMJ preservation and reinnervation in the N+B group.

3.4.7. Dynamic monitoring of sciatic nerve function index after surgery

The SFI was used to dynamically evaluate locomotor recovery over 4 weeks. SFI remained near 0 in the Sham group, indicating normal function, while the PNI group showed persistently low SFI values (~ −100), reflecting complete functional loss.

In the first postoperative week, all groups except the Sham group exhibited a sharp decline in SFI. From weeks 2 to 4, functional recovery in the N+B group accelerated significantly compared to the NRG1 and B-dSC groups, which showed moderate improvement, whereas the PNI group showed no meaningful recovery (Figures A1C and 8G).

3.4.8. Electrophysiology

Electrophysiological recordings were conducted to assess functional myelin integrity via CV, LT, and compound muscle action potential amplitude. 4 weeks after surgery, the N+B group exhibited superior neural function (CV: 104 ± 3m/s; LT: 6.0 ± 0.4ms; AP: 2.41 ± 0.14mV) compared to the PNI (CV: 13 ± 3m/s; LT: 12.8 ± 0.8ms; AP: 0.79 ± 0.08mV), NRG1 (CV: 53 ± 6m/s; LT: 10.9 ± 0.7ms; AP: 1.45 ± 0.05mV), and B-dSC (CV: 63 ± 6m/s; LT: 9.0 ± 0.7ms; AP: 1.78 ± 0.05mV) groups.

While still slightly inferior to the Sham group (CV: 115 ± 5m/s; LT: 3.3 ± 0.2ms; AP: 2.88 ± 0.07mV), the NRG1+B group demonstrated robust electrophysiological recovery ($p < 0.05$) (Figure 8H–J).

3.4.9. Sciatic nerve magnetic resonance imaging

T2-weighted MRI was employed to visualize structural recovery. In the PNI group, the injury site appeared as a hypointense gap ("black void") on the nerve pathway. In contrast, the N+B and other treated groups showed filling of the injury region with regenerated nerve tissue. However, the signal intensity remained slightly lower than that of native nerve tissue, indicating ongoing remodeling (Figure 8K).

4. Discussion

Dedifferentiation is a crucial prerequisite for myelin regeneration and nerve repair following PNI.[8,41] The limited dedifferentiation capacity of B-dSCs restricts their potential to effectively replace ASCs in PNI repair.[7] To enhance the dedifferentiation of B-dSCs and improve their myelination capabilities *in vivo*, we applied NRG1, a widely recognized inducer of Schwann cell dedifferentiation, to a B-dSC and DRG neuron co-culture system. Our observations revealed an upregulation in the expression of both dedifferentiation markers and myelin markers, suggesting that NRG1 can drive B-dSCs into a dedifferentiation-myelin regeneration phase. This finding implies that NRG1 may enhance the myelination ability of B-dSCs by promoting their dedifferentiation, although further *in vivo* studies are required to validate this.

Given that transection-type PNIs necessitate prolonged recovery periods and extensive regeneration distances, it is essential to employ a suitable delivery carrier capable of bridging nerve stumps while providing sustained and localized release of NRG1. Although hydrogels and other biomaterials have been widely employed as NRG1 delivery vehicles *in vivo*,[42,43] they generally fail to maintain therapeutic concentrations of NRG1 over

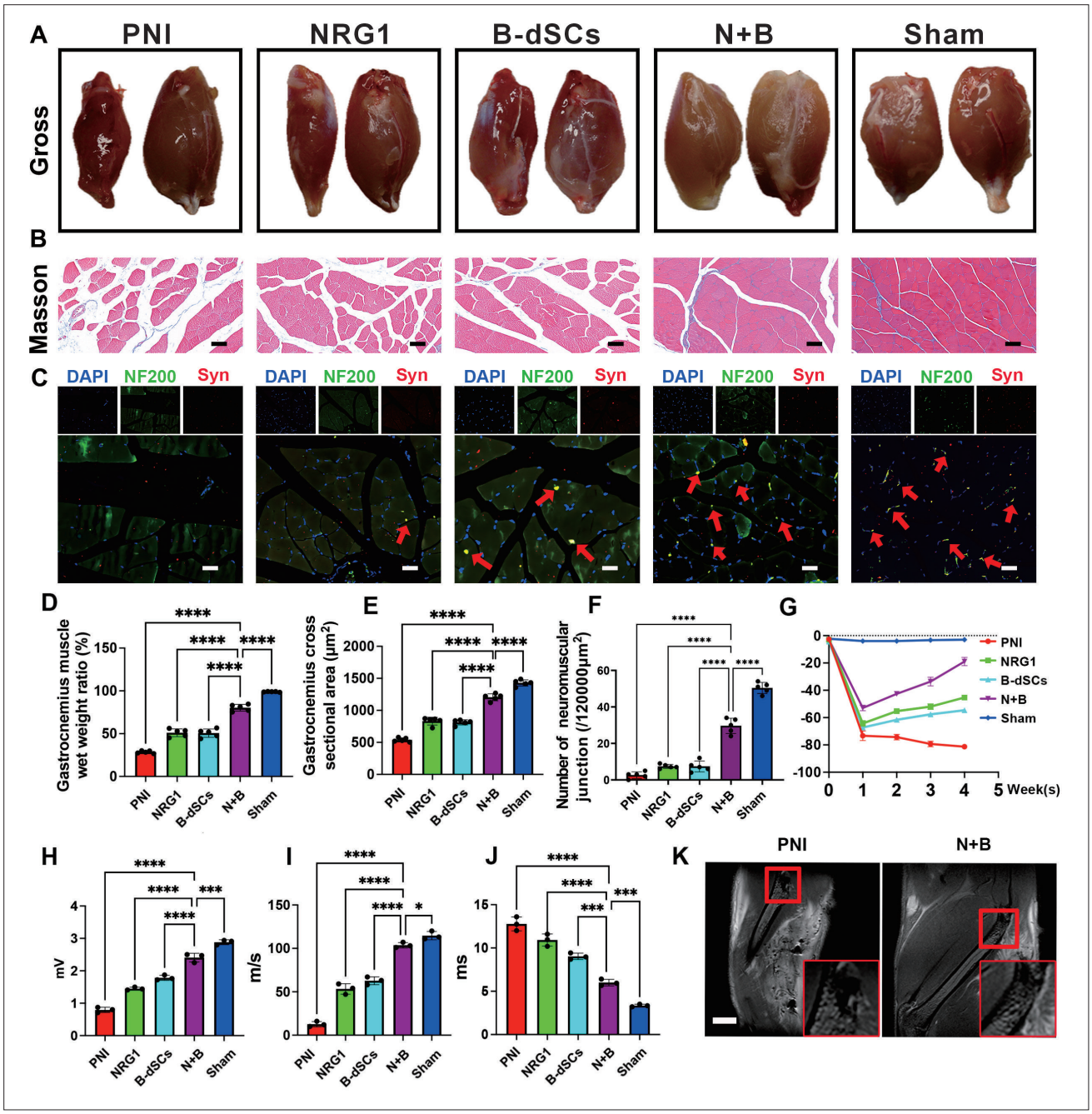

Figure 8. Assessments related to regenerated nerve function. (A) Gross images of the gastrocnemius muscle, comparing the injured side (left) with the normal side (right). (B) Masson staining of gastrocnemius muscle cross-sections, revealing differences in muscle fiber density. (C) Fluorescence staining of neurofilaments (green) and synapses (red) in gastrocnemius muscle sections, indicating neuromuscular junction density. Red arrows point to synapses in muscle tissue. (D) Quantification of the relative wet weight of the gastrocnemius muscle, showing less atrophy in the N+B group. (E) Quantification of gastrocnemius muscle cross-sectional area, indicating reduced muscle atrophy in the N+B group. (F) Quantification of neuromuscular junction density in the gastrocnemius muscle, showing higher density in the N+B group. (G) Quantification of the SFI, demonstrating faster functional recovery in the N+B group. (H) Quantification of the regenerated nerve electrical signal, showing greater signal strength in the N+B group. (I) Quantification of conduction velocity of the regenerated nerve electrical signal, with improved conduction in the N+B group. (J) Quantification of latency of the regenerated nerve electrical signal, indicating faster signal transmission in the N+B group. (K) Magnetic resonance images of nerve repair, highlighting the extent of structural recovery in the N+B group. Red boxes show corresponding magnified views. $^{*}p < 0.05$; $^{***}p < 0.001$; $^{****}p < 0.0001$. One-way analysis of variance with Tukey's post hoc test. Scale bars: (B) = 30 μm; (C) = 50 μm. Magnifications: (B) = 200×; (C) = 100×. *Note*: N+B: (NRG1 + B-dSCs) + dorsal root ganglion co-culture. Abbreviations: B-dSCs, bone marrow-derived Schwann-like cells; DAPI, 4',6-diamidino-2-phenylindole; NF200, neurofilament heavy; NRG1, neuregulin-1; PNI, peripheral nerve injury; SFI, sciatic nerve function index; Syn, synaptophysin.

extended periods. While SRMs can prolong NRG1 release, traditional hydrogel matrices embedding these microspheres often lack structural constraints, leading to microsphere sedimentation and aggregation due to gravity, and thus creating uneven distributions (Figure 1I). This unevenness results in significant local variations in NRG1 concentration.

To address this challenge, we utilized advanced 3D-printing technology to fabricate highly interconnected, grid-like hydrogel scaffolds that effectively confine NRG1-SRMs within the hydrogel fibers. This architectural design minimized microsphere mobility and prevented sedimentation, maintaining a uniform distribution of NRG1 after printing and ensuring stable local concentrations.

In vivo experiments demonstrated that NRG1 initiated robust axonal regeneration, markedly increasing the number of small-diameter axons. Concurrently, the hydrogel scaffold facilitated axonal growth through its intrinsic porous structure. Furthermore, 3D printing significantly increased the hydrogel's surface area, enabling NRG1 to diffuse effectively into scaffold pores and maintain optimal concentrations around regenerating axons, thereby promoting extensive axonal elongation and regeneration.

In vivo fluorescence tracing of B-dSCs embedded within 3D-NRG1-SRM scaffolds confirmed early-stage expression of dedifferentiation-associated proteins induced by NRG1 treatment. *In vitro* experiments corroborated these findings, demonstrating that NRG1 induced B-dSCs to adopt a bipolar spindle-shaped morphology and significantly enhanced cell motility, indicating effective dedifferentiation. Enhanced motility enabled dedifferentiated B-dSCs to rapidly migrate toward regenerating axons, forming tube-like structures analogous to bands of Büngner that guide axonal growth. Following axonal regeneration, the superior remodeling capabilities of dedifferentiated B-dSCs facilitated radial sorting and subsequent myelin sheath formation around axons. Notably, the initiation of radial sorting depends on axonal diameter, with dedifferentiated B-dSCs preferentially myelinating larger-diameter axons while bundling smaller axons into Remak fibers.[44] Without dedifferentiated B-dSCs, NRG1 alone increased axon numbers, but these were predominantly small-diameter axons exhibiting sparse myelination. Conversely, introducing dedifferentiated B-dSCs substantially increased axon diameter, prompting B-dSC-mediated radial sorting and robust myelination rather than Remak fiber formation. These results suggest that enhanced myelination primarily arises indirectly through dedifferentiated B-dSC-induced increases in axonal diameter, rather than direct NRG1 action alone. This finding further emphasizes the importance of integrating supportive seed cells to achieve effective myelin regeneration post-PNI.

Mechanistically, the dedifferentiation process of B-dSCs appears closely linked to the JNK signaling pathway, which is critically involved in Schwann cell dedifferentiation.[26,45] Activation of the JNK pathway promotes the expression of dedifferentiation-associated proteins, induces morphological changes, and enhances Schwann cell motility.[46] Our findings indicate significant JNK pathway activation in dedifferentiated B-dSCs following NRG1 treatment, while pharmacological inhibition of JNK markedly suppressed NRG1-induced dedifferentiation and myelin gene expression. These results suggest that NRG1 facilitates the myelination capability of B-dSCs by activating the JNK signaling cascade, thereby altering the biological and functional properties of these cells.

Moreover, we observed that insufficient myelination correlated with reduced NMJ formation and subsequent muscle atrophy, possibly due to disrupted nerve impulse conduction, leaving muscles in disuse. Interestingly, despite relatively better axon regeneration, the NRG1-alone group exhibited poor electrophysiological recovery and pronounced muscle atrophy. This finding highlights that intact myelination, in addition to axonal regeneration, is critical for maintaining functional neuromuscular connectivity. MRI further supported the beneficial effects of dedifferentiated B-dSCs in nerve structural restoration and prevention of muscle atrophy, providing valuable insights for future clinical translation.

5. Conclusion

NRG1 effectively promotes B-dSC dedifferentiation, significantly enhancing their myelination capacity *in vivo*. The spatial precision afforded by 3D-printing technology, combined with the sustained-release properties of microspheres, ensures stable, prolonged, and homogeneous NRG1 delivery. Together, this integrated biomaterial and biological approach offers a promising therapeutic strategy for promoting nerve and myelin regeneration following PNI.

Acknowledgments

None.

Funding

This research was supported by the National Natural Science Foundation of China (Grant No. 82201785), the Guangdong Basic and Applied Basic Research Foundation (supported by the Medical Scientific Research Foundation of Guangdong Province, China, Grant No. 20241120250;

A2025267), the Provincial Enterprise Joint Fund—General Project (Grant No. 2022A1515220046), Guangzhou City-University (Institute)-Enterprise Joint Funding Project (Grant No. SL2023A03J00448) as well as Science and Technology Projects in Guangzhou and the City-University (Institute) Enterprise Joint Funded Project (Grant Nos. 202201020633; 2024A03J0277).

Conflict of interest

The authors declare no potential conflicts of interest with respect to the research, authorship, and/or publication of this article.

Author contributions

Conceptualization: Bo Hou, Guanhua Zhang
Formal analysis: Bo Hou, Enpeng Song
Investigation: Bo Hou, Enpeng Song, Peng Yu, Jie Wei
Methodology: Bo Hou, Jie Liu
Writing–original draft: Guanhua Zhang
Writing–review & editing: Guanhua Zhang, Yaqiong Wang, Jie Liu

Ethics approval and consent to participate

All experimental procedures were approved by the Institutional Animal Care and Use Committee (IACUC) of Sun Yat-sen University (approval number SYSU-IACUC-2023-000125; [11/30/2023]) and conducted in accordance with the Guide for the Care and Use of Laboratory Animals issued by the Chinese Institute of Health.

Consent for publication

Not applicable.

Availability of data

The datasets generated and analyzed during the current study are available from the corresponding author upon reasonable request.

References

1. Zhang Y, Yi D, Hong Q, et al. Platelet-rich plasma-derived exosomes boost mesenchymal stem cells to promote peripheral nerve regeneration. *J Control Release*. 2024;367(2):265-282.
doi: 10.1016/j.jconrel.2024.01.043.

2. Dai Y, Lu T, Li L, et al. Electrospun composite PLLA-PPSB nanofiber nerve conduits for peripheral nerve defects repair and regeneration. *Adv Healthc Mater*. 2024;13(10):e2303539.
doi: 10.1002/adhm.202303539.

3. Rodríguez FJ, Verdú E, Ceballos D, Navarro X. Nerve guides seeded with autologous schwann cells improve nerve regeneration. *Exp Neurol*. 2000;161(2):571-584.
doi: 10.1006/exnr.1999.7315.

4. Bachelin C, Lachapelle F, Girard C, et al. Efficient myelin repair in the macaque spinal cord by autologous grafts of Schwann cells. *Brain*. 2005;128(3):540-549.
doi: 10.1093/brain/awh406.

5. Sun X, Zhu Y, Yin HY, et al. Differentiation of adipose-derived stem cells into Schwann cell-like cells through intermittent induction: potential advantage of cellular transient memory function. *Stem Cell Res Ther*. 2018;9:133.
doi: 10.1186/s13287-018-0884-3.

6. Wei C, Guo Y, Ci Z, Li M, Zhang Y, Zhou Y. Advances of Schwann cells in peripheral nerve regeneration: from mechanism to cell therapy. *Biomed Pharmacother*. 2024;175:116645.
doi: 10.1016/j.biopha.2024.116645.

7. Hou B, Ye Z, Ji W, et al. Comparison of the effects of BMSC-derived Schwann cells and autologous Schwann cells on remyelination using a rat sciatic nerve defect model. *Int J Biol Sci*. 2018;14(14):1910-1922.
doi: 10.7150/ijbs.26765.

8. Li R, Li D, Wu C, et al. Nerve growth factor activates autophagy in Schwann cells to enhance myelin debris clearance and to expedite nerve regeneration. *Theranostics*. 2020;10(4):1649-1677.
doi: 10.7150/thno.40919.

9. Kataria H, Alizadeh A, Karimi-Abdolrezaee S. Neuregulin-1/ErbB network: an emerging modulator of nervous system injury and repair. *Prog Neurobiol*. 2019;180:101643.
doi: 10.1016/j.pneurobio.2019.101643.

10. Soto J, Monje PV. Axon contact-driven Schwann cell dedifferentiation. *Glia*. 2017;65(6):864-882.
doi: 10.1002/glia.23131.

11. Li X, Zhang T, Li C, et al. Electrical stimulation accelerates Wallerian degeneration and promotes nerve regeneration after sciatic nerve injury. *Glia*. 2023;71(4):758-774.
doi: 10.1002/glia.24309.

12. Stoll G, Müller HW. Nerve injury, axonal degeneration and neural regeneration: basic insights. *Brain Pathol*. 1999;9(2):313-325.
doi: 10.1111/j.1750-3639.1999.tb00229.x.

13. Ding Z, Dai C, Shan W, et al. TNF-α up-regulates Nanog by activating NF-κB pathway to induce primary rat spinal cord astrocytes dedifferentiation. *Life Sci*. 2021;287:120126.
doi: 10.1016/j.lfs.2021.120126.

14. Boerboom A, Reusch C, Pieltain A, Chariot A, Franzen R. KIAA1199: a novel regulator of MEK/ERK-induced Schwann cell dedifferentiation. *Glia*. 2017;65(10):1682-1696.
doi: 10.1002/glia.23188.

15. Honorati MC, Cattini L, Facchini A. IL-17, IL-1beta and TNF-alpha stimulate VEGF production by dedifferentiated chondrocytes. *Osteoarthritis Cartilage*. 2004;12(8):683-691. doi: 10.1016/j.joca.2004.05.009.

16. Dinarello CA. Proinflammatory cytokines. *Chest*. 2000;118(2):503-508. doi: 10.1378/chest.118.2.503.

17. Jayaraman T, Paget A, Shin YS, et al. TNF-alpha-mediated inflammation in cerebral aneurysms: a potential link to growth and rupture. *Vasc Health Risk Manag*. 2008;4:805-817. doi: 10.2147/vhrm.s2700.

18. Zhou Y, Xu Z, Liu Z. Role of IL-33-ST2 pathway in regulating inflammation: current evidence and future perspectives. *J Transl Med*. 2023;21:902. doi: 10.1186/s12967-023-04782-4.

19. Min B, Kim D, Feige MJ. IL-30(†) (IL-27A): a familiar stranger in immunity, inflammation, and cancer. *Exp Mol Med*. 2021;53:823-834. doi: 10.1038/s12276-021-00630-x.

20. Wang P, Qian H, Xiao M, Lv J. Role of signal transduction pathways in IL-1β-induced apoptosis: pathological and therapeutic aspects. *Immun Inflamm Dis*. 2023;11(5):e762. doi: 10.1002/iid3.762.

21. Kang R, Li R, Dai P, Li Z, Li Y, Li C. Deoxynivalenol induced apoptosis and inflammation of IPEC-J2 cells by promoting ROS production. *Environ Pollut*. 2019;251:689-698. doi: 10.1016/j.envpol.2019.05.026.

22. Newbern J, Birchmeier C. Nrg1/ErbB signaling networks in Schwann cell development and myelination. *Semin Cell Dev Biol*. 2010;21(8-9):922-928. doi: 10.1016/j.semcdb.2010.08.008.

23. Birchmeier C. ErbB receptors and the development of the nervous system. *Exp Cell Res*. 2009;315(4):611-618. doi: 10.1016/j.yexcr.2008.10.035.

24. Boerboom A, Dion V, Chariot A, Franzen R. Molecular mechanisms involved in Schwann cell plasticity. *Front Mol Neurosci*. 2017;10:38. doi: 10.3389/fnmol.2017.00038.

25. Fornasari BE, El Soury M, Nato G, et al. Fibroblasts colonizing nerve conduits express high levels of soluble neuregulin1, a factor promoting schwann cell dedifferentiation. *Cells*. 2020;9(6):1366. doi: 10.3390/cells9061366.

26. Monje PV, Soto J, Bacallao K, Wood PM. Schwann cell dedifferentiation is independent of mitogenic signaling and uncoupled to proliferation: role of cAMP and JNK in the maintenance of the differentiated state. *J Biol Chem*. 2010;285(42):31024-31036. doi: 10.1074/jbc.M110.116970.

27. Kong L, Hassinan CW, Gerstner F, et al. Boosting neuregulin 1 type-III expression hastens SMA motor axon maturation. *Acta Neuropathol Commun*. 2023;11:53. doi: 10.1186/s40478-023-01551-8.

28. Michailov GV, Sereda MW, Brinkmann BG, et al. Axonal neuregulin-1 regulates myelin sheath thickness. *Science*. 2004;304(5671):700-703. doi: 10.1126/science.1095862.

29. Kim H, Park H, Lee SJ. Effective method for drug injection into subcutaneous tissue. *Sci Rep*. 2017;7:9613. doi: 10.1038/s41598-017-10110-w.

30. Yin PT, Han E, Lee KB. Engineering stem cells for biomedical applications. *Adv Healthc Mater*. 2016;5(1):10-55. doi: 10.1002/adhm.201400842.

31. Liu L, Wannemuehler MJ, Narasimhan B. Biomaterial nanocarrier-driven mechanisms to modulate anti-tumor immunity. *Curr Opin Biomed Eng*. 2021;20:100322. doi: 10.1016/j.cobme.2021.100322.

32. Gutierrez AM, Frazar EM, Klaus MVX, Paul P, Hilt JZ. Hydrogels and hydrogel nanocomposites: enhancing healthcare through human and environmental treatment. *Adv Healthc Mater*. 2022;11(2):e2101820. doi: 10.1002/adhm.202101820.

33. Qian Y, Lu S, Meng J, Chen W, Li J. Thermo-responsive hydrogels coupled with photothermal agents for biomedical applications. *Macromol Biosci*. 2023;23(3):e2300214. doi: 10.1002/mabi.202300214.

34. Gu D, O'Connor AJ, Qiao GHG, Ladewig K. Hydrogels with smart systems for delivery of hydrophobic drugs. *Expert Opin Drug Deliv*. 2017;14(8):879-895. doi: 10.1080/17425247.2017.1245290.

35. Asadi N, Alizadeh E, Salehi R, Khalandi B, Davaran S, Akbarzadeh A. Nanocomposite hydrogels for cartilage tissue engineering: a review. *Artif Cells Nanomed Biotechnol*. 2018;46(6):465-471. doi: 10.1080/21691401.2017.1345924.

36. Buonanno A, Fischbach GD. Neuregulin and ErbB receptor signaling pathways in the nervous system. *Curr Opin Neurobiol*. 2001;11(2):287-296. doi: 10.1016/s0959-4388(00)00210-5.

37. Jorissen RN, Walker F, Pouliot N, Garrett TPJ, Ward CW, Burgess AW. Epidermal growth factor receptor: mechanisms of activation and signalling. *Exp Cell Res*. 2003; 284(1):31-53. doi: 10.1016/s0014-4827(02)00098-8.

38. Wen J, Hou B, Lin W, et al. 3D-printed hydrogel scaffold-loaded granulocyte colony-stimulating factor sustained-release microspheres and their effect on endometrial regeneration. *Biomater Sci*. 2022;10(12):3346-3358. doi: 10.1039/d2bm00109h.

39. Griffith LG, Naughton G. Tissue engineering—current challenges and expanding opportunities. *Science*. 2002;295(5557):1009-1014. doi: 10.1126/science.1069210.

40. Fraher JP. Myelin-axon relationships in the rat phrenic nerve: longitudinal variation and lateral asymmetry. *J Comp Neurol*. 1992;323(3):551-557.
doi: 10.1002/cne.903230407.

41. Su Q, Nasser MI, He J, et al. Engineered schwann cell-based therapies for injury peripheral nerve reconstruction. *Front Cell Neurosci*. 2022;16:865266.
doi: 10.3389/fncel.2022.865266.

42. Hui T, Wang C, Yu L, Zhou C, Qiu M. Phosphorene hydrogel conduits as "neurotrophin reservoirs" for promoting regeneration of peripheral nerves. *J Mater Chem B*. 2023;11(18):3808-3815.
doi: 10.1039/d3tb00340j.

43. Yasui G, Yamamoto Y, Shichinohe R, et al. Neuregulin-1 released by biodegradable gelatin hydrogels can accelerate facial nerve regeneration and functional recovery of traumatic facial nerve palsy. *J Plast Reconstr Aesthet Surg*. 2016;69(2):328-334.
doi: 10.1016/j.bjps.2015.10.037.

44. Jung N, Park S, Choi Y, et al. Tonsil-derived mesenchymal stem cells differentiate into a Schwann cell phenotype and promote peripheral nerve regeneration. *Int J Mol Sci*. 2016;17(11):1867.
doi: 10.3390/ijms17111867.

45. Shin YK, Jang SY, Park JY, et al. The neuregulin-Rac-MKK7 pathway regulates antagonistic c-jun/Krox20 expression in Schwann cell dedifferentiation. *Glia*. 2013;61(5):892-904.
doi: 10.1002/glia.22482.

46. Kaempchen K, Mielke K, Utermark T, Langmesser S, Hanemann CO. Upregulation of the Rac1/JNK signaling pathway in primary human schwannoma cells. *Hum Mol Genet*. 2003;12(10):1211-1221.
doi: 10.1093/hmg/ddg146.

Appendix

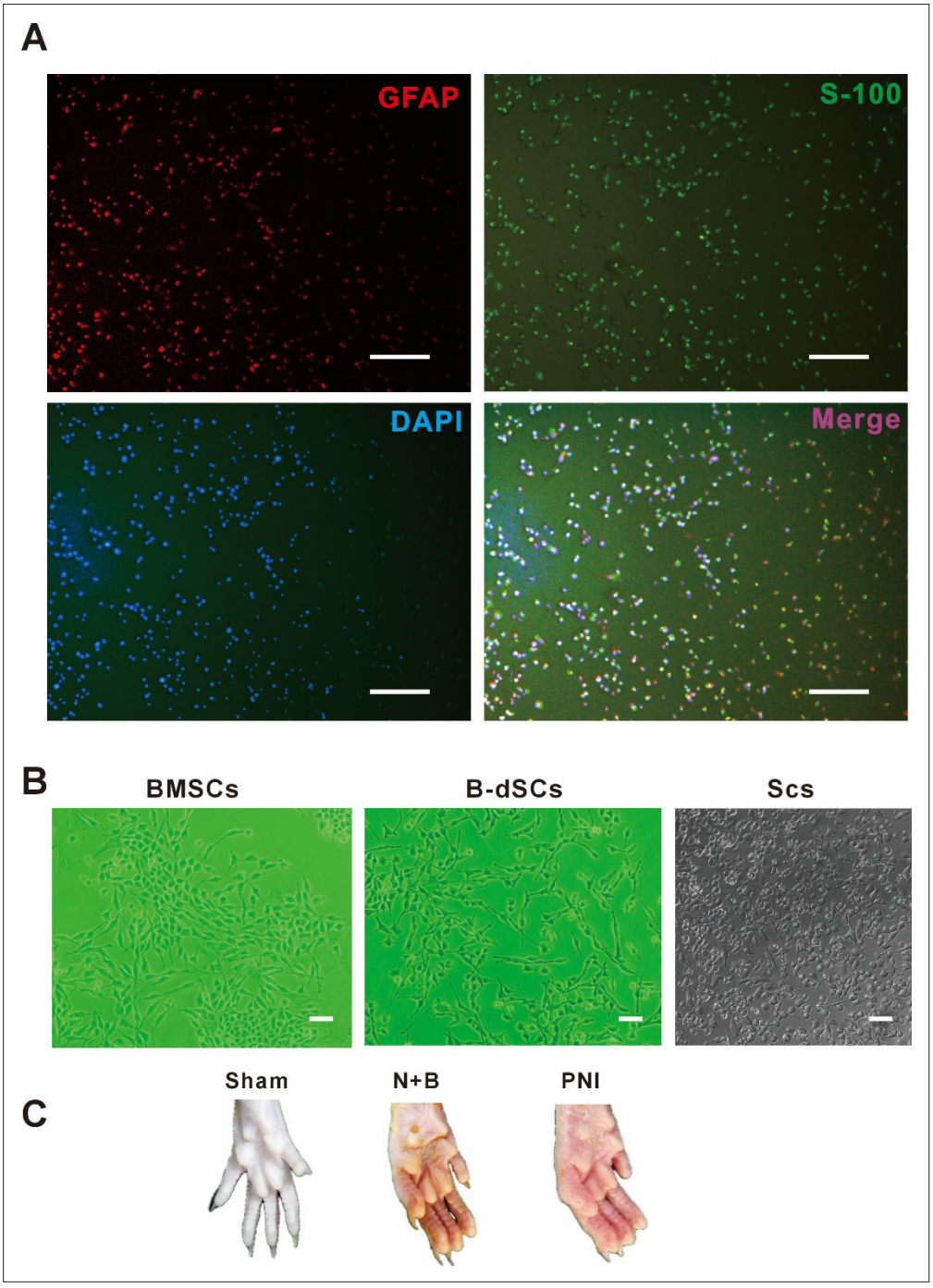

Figure A1. Characterization of B-dSCs and schematic images of rat hindlimbs at 4 weeks post-surgery. (A) Most B-dSCs positively expressed Schwann cell-specific markers, including S-100 and GFAP. (B) Compared to normal BMSCs, the induced B-dSCs displayed a disorganized cellular arrangement and a spindle-shaped morphology with elongated processes, resembling SCs. (C) Compared to the severe muscle atrophy and toenail loss in the PNI group, the N+B group showed only mild atrophy. Scale bars: (A) = 50 μm; (B) = 100 μm. **Magnifications:** (A) = **100**×; (B) = **100**×. *Note*: **N+B: (NRG1 + B-dSCs) + dorsal root ganglion co-culture.** Abbreviations: B-dSC, bone marrow-derived Schwann-like cell; BMSCs, bone marrow mesenchymal stem cells; DAPI, 4',6-diamidino-2-phenylindole; GFAP, glial fibrillary acidic protein; NRG1, neuregulin-1; PNI, peripheral nerve injury; SCs, Schwann cells.

Raw image file

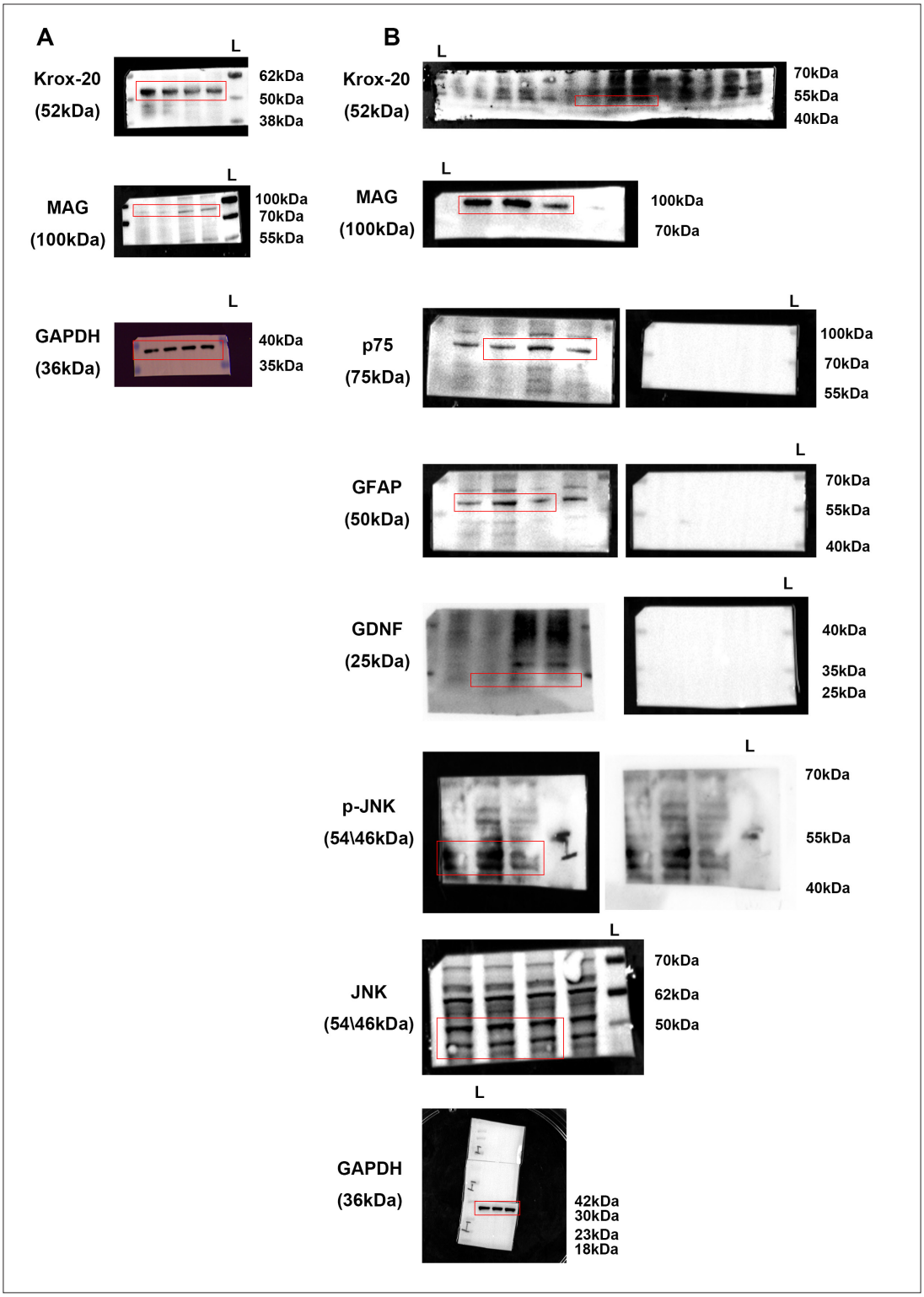

Figure R1. Raw images for Western blotting results in **Figure 3**. (A) Raw images for **Figure 3A**; (B) Raw images for **Figure 3B**.